

© Copyright 2017

Eleanor Sobocinski Johnson

# Cells Incognito: Microfluidic Tools for Detecting and Isolating Cancer Cells

Eleanor Sobocinski Johnson

A dissertation

submitted in partial fulfillment of the  
requirements for the degree of

Doctor of Philosophy

University of Washington

2017

Reading Committee:

Daniel T. Chiu, Chair

Bo Zhang

Dustin Maly

Program Authorized to Offer Degree:

Chemistry

University of Washington

**Abstract**

Cells Incognito: Microfluidic Tools for Detecting and Isolating Cancer Cells

Eleanor Sobocinski Johnson

Chair of the Supervisory Committee:  
Professor Daniel T. Chiu  
Chemistry

Cancer continues to be one of the leading causes of death around the world. The disease is characterized by uncontrolled cell growth and is spread throughout the body by the dissemination of cancer cells into circulation. These cells contain the mutations that caused the original tumor and can seed metastases in distant sites. Most cancer deaths result from metastasis and preventing this is vital to developing an effective cure. Detecting and isolating the cells that spread disease can facilitate this by making these cells accessible to researchers.

Heterogeneity among cancer cells necessitates the study of single cells. This heterogeneity is thought to be critical to progress in cancer treatment, since a subset of cells can evade detection and seed new metastases after the original cancer has been treated. While there has been a lot of work done to understand these dangerous and elusive cells, new tools are

needed to accurately isolate them from large cell populations. Microfluidic devices move detection to the microscale, allowing for precise detection and manipulation of individual cells.

In this thesis, work is presented on microfluidic devices to detect, isolate and manipulate cancer cells. There are three main projects discussed. The first is improved detection of the subpopulation of circulating tumor cells (CTCs) thought to be most likely to seed new tumors. These cells express low levels of epithelial markers after undergoing a physiological change, the epithelial-to-mesenchymal transition, which allows them to better survive in circulation. Detection is done on our in-house CTC isolation platform, ensemble decision aliquot ranking (eDAR). Next, a novel electrochemical cell trapping platform for isolation of single cells for analysis is discussed. This device utilizes bi-polar electrodes (BPEs) to create faradaic ionic enrichment (FIE) or depletion (FID) zones to manipulate cells. Finally, a microfluidic device for the isolation of circulating tumor cells is presented. This device is based on eDAR, but implements a sequential sorting scheme to improve purity (1% to 70%) and isolate the cells in a 96-well plate for downstream analysis.

# TABLE OF CONTENTS

List of Figures .....	v
List of Tables .....	vii
Chapter 1. Introduction.....	10
1.1 Overview.....	11
1.2 Circulating Tumor Cells .....	13
1.2.1 Epithelial-to-mesenchymal transition .....	13
1.3 eDAR .....	15
1.3.1 Device Design.....	15
1.3.2 Recoveries, Clinical Results and Limitations .....	17
Chapter 2. Improved Detection By Ensemble Decision Aliquot Ranking (Edar) Of Circulating Tumor Cells With Low Numbers Of A Targeted Surface Antigen .....	18
2.1 Abstract.....	19
2.2 Introduction.....	20
2.3 Methods.....	24
2.3.1 Cell culture.....	24
2.3.2 Clinical samples.....	24
2.3.3 Reagents.....	25
2.3.4 Microfluidic chips.....	25
2.3.5 Flow cytometry.....	25
2.3.6 eDAR detection of spiked-in cultured cells.....	26

2.3.7	eDAR isolation of CTCs from patient-derived samples. ....	27
2.4	Results And Discussion .....	29
2.4.1	eDAR detection of a model EpCAM <sup>low</sup> cell line. ....	29
2.4.2	Quantitative approach to eDAR recovery efficiency.....	33
2.4.3	6-fold increased recovery of CTCs from patient-derived samples. ....	38
2.5	Conclusion .....	39
2.6	Supporting Information.....	40
2.6.1	Parametric evaluation of measured signal intensity and signal-to-noise ratio in eDAR. ....	40
2.6.2	Isotype control experiments.....	42
2.6.3	eDAR calibration. ....	43
Chapter 3. Negative Dielectrophoretic Capture and Repulsion of Single Cells at a Bipolar Electrode: The Impact of Faradaic Ion Enrichment and Depletion .....		
		45
3.1	Abstract.....	46
3.2	Introduction.....	46
3.3.1	Bipolar Electrochemistry .....	50
3.3.2	Generation of Faradaic Ion Enrichment and Depletion (FIE and FID) Zones .....	51
3.3.3	DEP Manipulation of Cells Using BPEs .....	53
3.4	Materials And Methods.....	57
3.4.1	Chemicals.....	57
3.4.2	Cell Culture.....	57
3.4.3	Device Fabrication .....	58
3.4.4	DEP Experiments.....	59

3.5	Results And Discussion .....	59
3.5.1	nDEP at a BPE in the Absence of Faradaic Reactions .....	60
3.5.2	nDEP Attraction of a B-Cell to an FIE Zone at the BPE Anode and the BPE Cathode .....	65
3.5.3	nDEP Repulsion of a B-Cell from an FID Zone.....	69
3.6	Conclusion .....	72
Chapter 4. Isolation of Circulating Tumor Cells from Whole Blood with High Purity Using a Sequential Sorting Scheme .....		
4.1	Abstract.....	74
4.2	Introduction.....	75
4.3	Materials And Methods.....	78
4.3.1	Cell culture.....	78
4.3.2	Blood samples.....	78
4.3.3	Reagents.....	78
4.3.4	Microfluidic chips.....	79
4.3.5	Testing of sequential sorting chip designs for dye stretching.....	79
4.3.6	Purity tests with sequential eDAR.....	80
4.3.7	Sequential eDAR recoveries.....	80
4.4	Results And Discussion .....	81
4.4.1	Two-stage sorting improves purity.....	81
4.4.2	Lengthening the channel between the two sorting junctions can improve the purity... .....	83

4.4.3	Manipulating the channel between the two sorting junctions can improve the purity.	84
4.4.4	Cells can be collected and enumerated in a 96-well plate.	89
4.5	Conclusion	92
	Bibliography	93

## LIST OF FIGURES

### Chapter 1

- Figure 1.1 Summary of the metastatic process.....14
- Figure 1.2 Microfluidic chip and hydrodynamic switching scheme of eDAR.....16

### Chapter 2

- Figure 2.1 eDAR Sorting Scheme.....22
- Figure 2.2 Comparison of eDAR labeling schemes.....30
- Figure 2.3 Calibration of eDAR.....34
- Figure 2.4 Cells from breast cancer clinical samples sorted on an eDAR chip.....37
- Figure 2.5 Impact of antibody concentration on eDAR detection.....40
- Figure 2.6 Isotype control experiments.....42
- Figure 2.7 Summary of MDA-MB-231 Labeling Results.....43

### Chapter 3

- Figure 3.1 Microfluidic Devices Comprising a Bipolar Electrode.....51
- Figure 3.2 Principles of nDEP Repulsion.....53
- Figure 3.3 nDEP repulsion of a B-cell under AC only field.....61
- Figure 3.4 nDEP attraction of a B-cell toward the BPE anode.....64
- Figure 3.5 nDEP repulsion from an FID zone at the BPE cathode.....68
- Figure 3.6 nDEP and EP from an FID zone at the BPE cathode.....70

### Chapter 4

- Figure 4.1 Detail of the sequential eDAR chip.....82

Figure 4.2 Different designs tested to stretch the eDAR aliquot.....85

Figure 4.3 Images of weir filter tests.....86

Figure 4.4 Scheme of the herringbone structure employed in the sequential sorting  
chip.....87

Figure 4.5 Images of the sequential sorting fluidics scheme.....90

Figure 4.6 Images of sorted clusters.....91

## LIST OF TABLES

Table 3.1	Effect of Electric Field Gradient Length on $F_{\text{DEP}}$ .....	56
Table 4.1	Purity results for sequential eDAR designs.....	89

## **ACKNOWLEDGEMENTS**

I would like to first thank my family, especially my parents and my sister, for being there for me through all the trials life has thrown my way and always emphasizing the importance of education. I am truly honored to be a part of such an amazing family.

I would also like to thank my advisor, Professor Daniel Chiu, and all the members of the Chiu lab who have supported me through all the years: Gloria Yen, Alison Thompson, Bryant Fujimoto, Thomas Schneider, Li Wu, and all the others. I am especially grateful to Robbyn Anand, for helping me when I was deep in the graduate school blues, and for being an amazing friend and mentor.

Finally, I would like to thank my Lord and Savior Jesus Christ, who used the trials and tribulations of graduate school to bring into relationship with Him and His Church.

## CHAPTER CONTRIBUTIONS

Chapter 2 of this dissertation is a published manuscript from Analytical Chemistry. I am the primary author and wrote the majority of the manuscript. Dr. Anand contributed portions of the writing. Much of the work was conducted in collaboration with Dr. Anand, who helped with experiment design and implementation, as well as data analysis. All authors contributed to editing the final manuscript. The published writing in this Chapter has been reproduced with permissions from the authors and Analytical Chemistry.

Chapter 3 of this dissertation is a published manuscript from the Journal of the American Chemical Society. I am the second author, and contributed to much of the work. The primary author, Dr. Anand, implemented the work and wrote the majority of the paper. I contributed to writing the materials and methods section and designing figures. Scientifically, I contributed to experimental design and implementation. All authors contributed to editing the final manuscript. The published writing in this Chapter has been reproduced with permissions from the authors and the Journal of the American Chemical Society.

Chapter 4 contains unpublished work and is in progress. I conducted the majority of the experiments and wrote the chapter. Dr. Zhao and Dr. Fujimoto contributed to the design of the device and instrumentation. Dr. Zhao implemented the project.

Chapter 1.

INTRODUCTION

“It's a dangerous business, Frodo, going out your door. You step onto the road, and if you don't keep your feet, there's no knowing where you might be swept off to.”

J.R.R. Tolkein, *The Lord of the Rings*

## 1.1 OVERVIEW

Cancer, one of the leading causes of death in America, is a disease which often eludes treatment or resurfaces after years of remission. The disease has complicated origins, with both genetic and environmental factors playing a role, and is characterized by uncontrolled growth of the patients own cells. These factors present a great need for more research so better treatments can be developed. Since cancer is a disease involving subpopulations of cells, isolating and manipulating cancer cells is of prime importance for research progress. This dissertation explores the development of tools for isolating cancer cells from whole blood and capturing single cells for study.

The tools described in this dissertation use microfluidics to accomplish rapid, precise analysis. Microfluidic devices allow small volumes to be interrogated in channels measuring tens to hundreds of microns in width. Two specific uses of microfluidics are discussed. The first describes a device for isolating circulating tumor cells (CTCs) from the blood of cancer patients. The second describes a microfluidic device for isolating single cells using electric fields. Both devices can give biologists new tools to answer the questions about cancer needed to develop new treatments.

Chapter 2 describes a critical improvement on our in-house CTC isolation platform, ensemble decision aliquot ranking (eDAR). eDAR was developed in our lab as a tool for isolating CTCs from whole blood, using fluorescent antibodies to detect cells of interest, which are then sorted on-chip with a fluidic sorting scheme. In previous work, the platform was validated with a variety of cultured cancer cell lines, as well as clinical samples. The

work presented here demonstrates a calibration of eDAR for a limit of detection (LOD) in terms of bound surface antibodies, an important metric for comparing between systems and estimating the detection of cells expressing low levels of epithelial surface markers. Also in this chapter is a description of a cocktail labeling scheme used to enhance our LOD and detect cells missed by other platforms.

Chapter 3 describes a microfluidic design for capturing single cells using dielectrophoresis (DEP). Cells flowing in a channel can be captured at certain points along the channel by generating faradaic ion enrichment and depletion (FIE and FID) zones. The device is fabricated with bi-polar electrodes (BPEs) aligned with small alcoves to capture the cells. This work presents a novel method of cell capture amenable to an array format that could be used to isolate single cells for downstream analysis techniques, such as polymerase chain reaction (PCR).

Chapter 4 describes work with a new eDAR device to improve purity and isolate cells for downstream analysis. This is accomplished with a sequential, on-chip sorting design where an aliquot of blood containing a cell of interest is sorted twice to improve purity and then collected in a 96-well plate to facilitate downstream analysis. In previous iterations of eDAR, the CTC was sorted into an aliquot of blood, which allowed for much faster sample processing than other fluorescent based methods, but limited purity. Incorporating another sorting junction on chip greatly improves purity without adding any additional processing time.

The next section of this introduction provides some background information on circulating tumor cells and a more in-depth description of eDAR.

## 1.2 CIRCULATING TUMOR CELLS

Circulating tumor cells are one of the leading cause of cancer metastasis, which is ultimately the cause of death in most cancers.<sup>1</sup> They present an important research avenue to understanding and treating cancer. CTCs are shed from the primary tumor and enter the blood stream, where they can travel to distant sites in the body and seed new tumors. These cells can be difficult to detect due to their low abundance<sup>2</sup> and heterogeneity.<sup>3</sup> This heterogeneity is due in part to the physiological change that occurs to enable survival in the blood stream.

### 1.2.1 *Epithelial-to-mesenchymal transition*

To survive in the blood, it is hypothesized that CTCs undergo a transition at the molecular level. This is called the epithelial-to-mesenchymal transition (EMT), and is characterized by the loss of epithelial markers and the acquisition of mesenchymal markers. Like many aspects of cancer, this process occurs normally under certain conditions, and is triggered in the disease state by activating already existing pathways.<sup>4</sup> Some of the changes that occur include loss of cell rigidity, increased motility, and a transition to a fibroblast-like shape.<sup>4</sup> The EMT is also characterized by the acquisition of mesenchymal markers (such as n-cadherin, vimentin, fibronectin) and the downregulation of epithelial markers (such as EpCAM, cytokeratin and E-cadherin).<sup>5</sup> These changes are summarized in Figure 1.1.

Understanding the EMT is of critical importance to detecting CTCs, since many methods target epithelial markers, with the most prevalent being epithelial cell adhesion molecule (EpCAM). The loss of rigidity and increased motility can also make the cells harder to detect by size-based methods, such filtration and flow fractionation. It is important to note that most CTC platforms use cultured epithelial cells as a standard, and these cells will not have undergone the

EMT like CTCs in patients. Many platforms also run samples from cancer patients, but it is difficult to know if there are CTCs being missed, since the CTCs detected are generally going to be the larger and more epithelial cells. Finally, it may be more important to isolate the more mesenchymal CTCs, since they have been linked to greater invasiveness.<sup>6</sup>

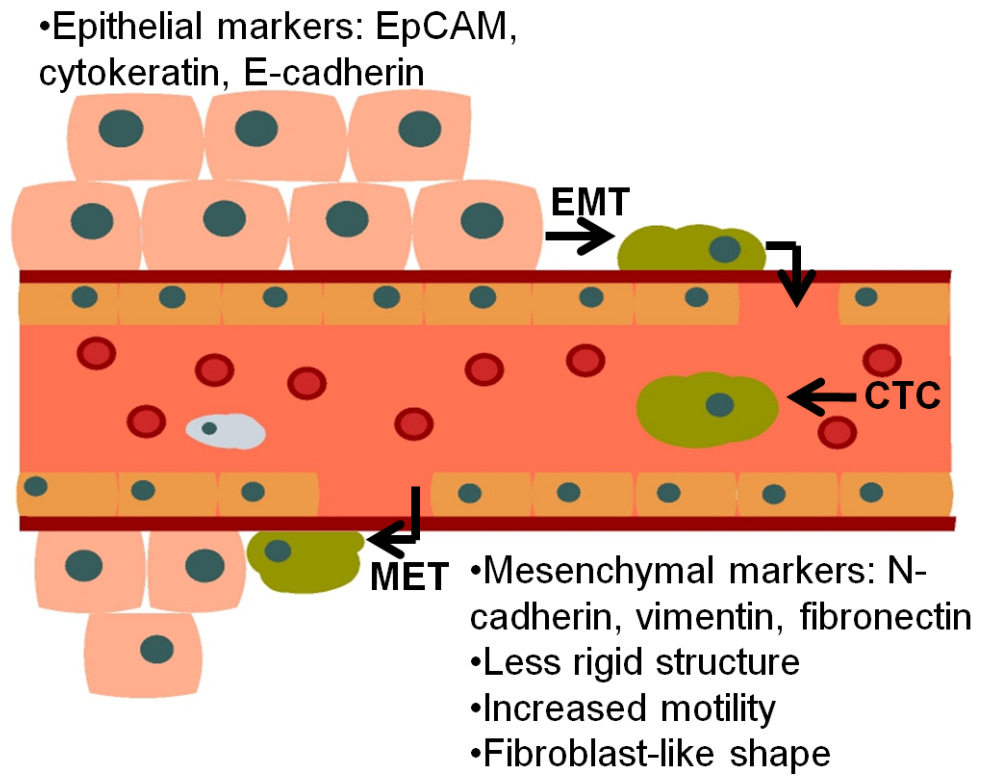


**Figure 1.1** Summary of the metastatic process, highlighting the physiological changes cells need to undergo to survive in circulation. The mesenchymal-to-epithelial transition (MET) is also shown.

## 1.3 eDAR

This dissertation will focus on two methods to improve the CTC isolation method, eDAR. Thus, a brief introduction will be given to previous work done develop the eDAR platform.

### 1.3.1 *Device Design*

eDAR uses a laser-induced fluorescence (LIF) detection method, implemented on a microfluidic chip mounted on an inverted microscope. Whole blood is labeled with fluorescent antibodies and flowed onto the chip. For CTC detection, the common epithelial cell adhesion marker (EpCAM) is used for detection. When a fluorescent cell passes the detection line, it triggers a sorting event, which causes an aliquot of blood to be sent down a collection channel (see Figure 1.2).<sup>7</sup> The sorting is controlled by a solenoid, which upon detection of a cell, opens an additional sheath flow channel controlled by P<sub>2</sub> in Figure 1.2 and the additional pressure from the right moves the flow to the left, thus sorting the aliquot.

The aliquot is sent to an on-chip filter with 5µm slits, where red blood cells and most white blood cells pass through and CTCs are retained for further analysis. Once cells have been captured on the filter, additional reagents for fixing and permeabilizing the cells can be flowed onto the chip, and cells can be labeled with additional antibodies. For CTC detection, cells are fixed, permeabilized, and labeled with Hoechst (a nuclear stain), cytokeratin (an intermediate filament protein found in epithelial cells), and CD45 (a protein common to all white blood cells). Cells positive for EpCAM, Hoechst and cytokeratin, and negative for CD45 are counted as CTCs.

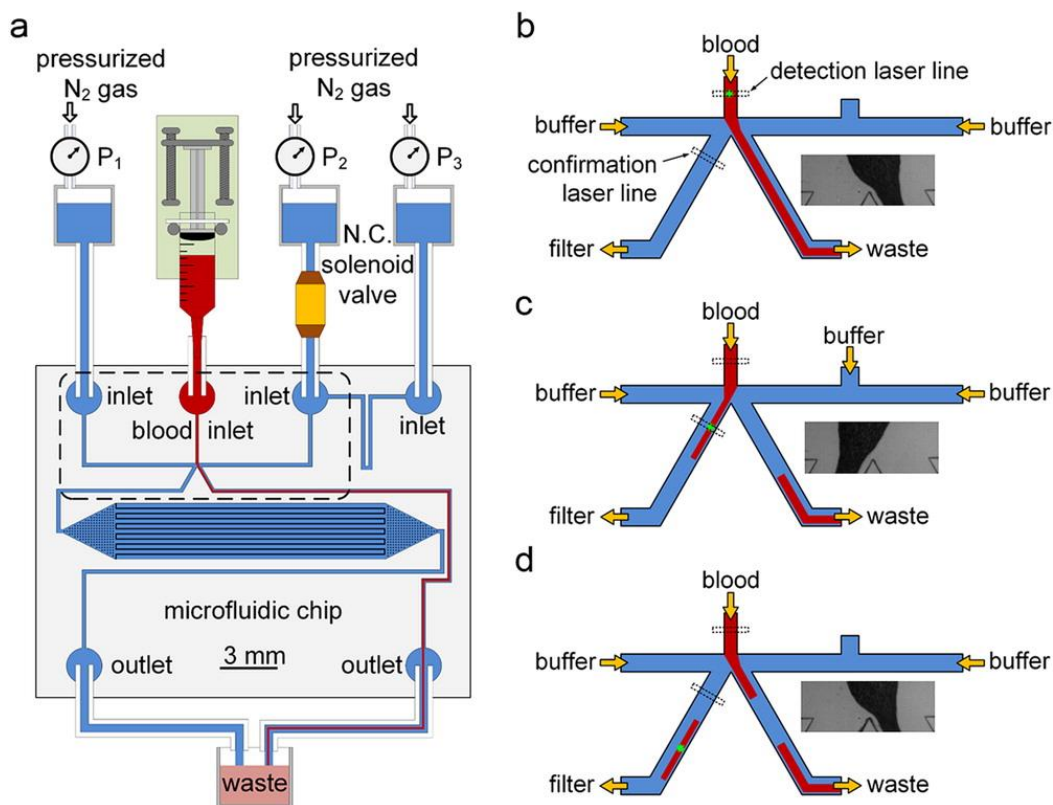


**Figure 1.2** Microfluidic chip and hydrodynamic switching scheme of eDAR. (a) General structure of the microfluidic chip and the configuration of the eDAR platform. The bottom left channel was to collect sorted aliquots and transfer them to the subsequent purification area, which had 20 000 microsits. The area marked with a dashed box is further explained in (b)–(d). (b) The flow condition when no positive aliquot was ranked. (c) The blood flow was switched to the CTC collection channel, and the sorted aliquot was confirmed by the second APD. (d) The blood flow was switched back after the aliquot was sorted.

Reprinted with permission from:

Zhao, M.; Nelson, W. C.; Wei, B.; Schiro, P. G.; Hakimi, B. M.; Johnson, E. S.; Anand, R. K.; Gyurkey, G. S.; White, L. M.; Samual, W. H.; Coveler, A. L.; Chiu, D. T. *Anal. Chem.* **2013**, *85* (20), 9671–9677. Copyright 2013 American Chemical Society.

### 1.3.2 *Recoveries, Clinical Results and Limitations*

Using this platform, previous researchers in our lab ran recoveries with spiked in cultured MCF7 cancer cells, obtaining greater than 95% recovery. Breast cancer cell lines MCF7, SKBr3 and MDA-MB-231 have all been tested on our platform. EpCAM, HER2 and EGFR were used as the detection antibody for each cell line respectively, and recoveries with all cell types exceeded 88%.<sup>7</sup> HER2 is a breast cancer marker found in about 30% of breast cancer patients, which is highly expressed on the SKBr3 cell line<sup>8</sup>. EGFR is an epidermal growth factor found to be overexpressed in some cancers.<sup>9</sup> These recoveries demonstrated the versatility of eDAR for different cell types while at the same time emphasizing a need for better labeling schemes to detect multiple cell types in the same sample.

Clinical samples from several different cancers were also run, including a comparison study against the FDA approved CTC isolation platform, CellSearch<sup>TM</sup>. More CTCs were consistently detected by eDAR than CellSearch<sup>TM</sup> for blood samples from the same patient (n=20)<sup>7</sup>. This is an important finding because, as mentioned earlier, there is a body of research suggesting that some CTCs may express low levels of EpCAM due to the epithelial-to-mesenchymal transition and go undetected by many platforms. These results demonstrate that the sensitivity of eDAR is higher than that of CellSearch<sup>TM</sup> and can detect some of these missed cells. However, eDAR was still using EpCAM to detect CTCs in clinical samples, and thus could still have been missing cells that could be important for understanding metastasis.

Chapter 2.

IMPROVED DETECTION BY ENSEMBLE  
DECISION ALIQUOT RANKING (EDAR) OF  
CIRCULATING TUMOR CELLS WITH LOW  
NUMBERS OF A TARGETED SURFACE  
ANTIGEN

*Reprinted with permission from*

Johnson, E. S.; Anand, R. K.; Chiu, D. T. Improved detection by ensemble decision aliquot ranking (eDAR) of circulating tumor cells with low numbers of a targeted surface antigen. *Anal. Chem.* **2015**, *87*, 9389–9395. Copyright 2015 American Chemical Society

## 2.1 ABSTRACT

Circulating tumor cells (CTCs) are shed from a solid tumor into the bloodstream and can seed new metastases. CTCs hold promise for cancer diagnosis and prognosis and to increase our understanding of the metastatic process. However, their low numbers in blood and varied phenotypic characteristics make their detection and isolation difficult. One source of heterogeneity among CTCs is molecular: When they leave the primary tumor, these cells must undergo a molecular transition, which increases their mobility and chance of survival in the blood. During this molecular transition, the cells lose some of their epithelial character, which is manifested by the expression of the cell surface antigen known as epithelial cell adhesion molecule (EpCAM). Some tumors shed CTCs that express high levels of EpCAM; others release cells that have a low level of the antigen. Nevertheless, many CTC isolation techniques rely on the detection of EpCAM to discriminate CTCs from other cells in the blood. We previously reported a high-throughput immunofluorescence-based technology that targets EpCAM to rank aliquots of blood for the presence or absence of a CTC. This technology, termed ensemble decision aliquot ranking (eDAR), recovered spiked-in cancer cells (taken from a model EpCAM<sup>high</sup> cell line) from blood at an efficiency of 95%. In this paper, we evaluated eDAR for recovery of cells that have low EpCAM expression and developed an immunofluorescence labeling strategy that significantly enhances the method's performance. Specifically, we used a

cocktail of primary antibodies for both epithelial and mesenchymal antigens as well as a dye-linked secondary antibody. The cocktail allowed us to reliably detect a model EpCAM<sup>low</sup> cell line for triple negative breast cancer, MDA-MB-231, with a recovery efficiency of 86%. Most significantly, we observed an average of 6-fold increase in the number of CTCs isolated from blood samples from breast cancer patients. These findings underscore the importance of benchmarking CTC technologies with model cell lines that express both high and low levels of EpCAM.

## 2.2 INTRODUCTION

Circulating tumor cells (CTCs) escape the primary tumor site and enter the bloodstream. As their presence has been linked with metastasis and reduced patient survival,<sup>1</sup> CTCs serve as an important diagnostic and prognostic tool. However, despite much research effort, the low levels in whole blood (<10 CTCs/ml),<sup>2,10,11</sup> combined with their heterogeneity,<sup>3</sup> has made it difficult to detect CTCs consistently in patients. There are several methods for detecting and isolating CTCs, including flow cytometry<sup>12-14</sup> immunomagnetic enrichment,<sup>15,16,3</sup> negative selection (depletion of white blood cells)<sup>17</sup>, and immunoaffinity binding.<sup>18-21</sup> Many detection methods take advantage of the epithelial origin of CTCs, which provides the cells with surface markers that are distinct from those on other cells in the blood. However, for a tumor cell to migrate into the bloodstream, it is reported to undergo an epithelial-to-mesenchymal transition (EMT), losing some of its epithelial characteristics, such as structural rigidity, cell adhesion and epithelial markers, such as EpCAM and cytokeratin, and taking on a more mesenchymal phenotype.<sup>4</sup> The phenotypic changes undergone by CTCs during the metastatic process mean that these cells may not express high levels of the epithelial markers, such as EpCAM, that are

targeted by current CTC detection techniques. These “EpCAM<sup>low</sup>” CTCs recently have received attention because they potentially can evade detection and have been linked with enhanced invasiveness and migration.<sup>6</sup> Accurate population statistics describing CTC expression of epithelial markers is unavailable. More importantly, immunoaffinity techniques traditionally quantify recovery rate (percentage of cells captured) using cultured cancer cells that are EpCAM<sup>high</sup> (e.g. the breast cancer cell line MCF-7) thus leading to an *upper estimate* of CTC recovery.

Size-based separation platforms have been developed as alternatives that do not depend on antigen expression.<sup>22–26</sup> These methods are based on the principle that CTCs are typically larger than other cells in circulation and can be separated using filtration. As with antibody-based techniques, these methods work well with cultured cells and show high recoveries with spiked-in cell samples. However, these recovery rates usually come at a loss of purity since the size distributions of cancer and white blood cells sometimes are not very well separated.<sup>27</sup> CTCs in patient samples are quite heterogeneous in both size and expression of surface antigens so all detection methods will be biased and cause some CTCs to be missed. Importantly, it is not possible to fully simulate this heterogeneity with cultured cells that have not undergone the EMT. There are different ways to account for inherent bias, but the antibody-based approach offers more attractive options for expanding detection.

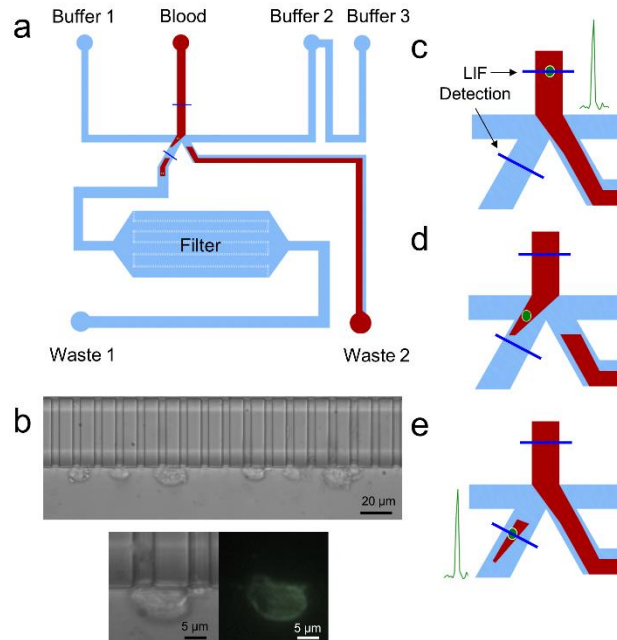


**Figure 2.1:** **a** An eDAR chip. The sample inlet (labeled “Blood”) led to two outlets for collection—a microfluidic filter (labeled “Filter”) for the capture of aliquots containing CTCs and a waste outlet for aliquots without CTCs (labeled “Waste 2”). A separate outlet (labeled “Waste 1”) served to keep a constant buffer flow across the filter area. The solid blue lines indicate the location of laser lines incident on the inlet channel (upper line) and collection channel (lower line) of the eDAR chip. These laser lines are used for laser-induced fluorescence (LIF) detection of fluorescently-tagged CTCs. **b** Images taken of PE-anti-EpCAM-labeled cultured cells (MCF-7) captured on the eDAR filter both in bright field (top and bottom left) and fluorescence (bottom right). The filter is used to retain the cells for visually confirming the identity of sorted cells of interest based on the expression of epithelial markers (EpCAM and cytokeratin), a nuclear stain (DAPI) and the absence of leukocyte marker (CD45) **c-d** An enhanced view of the eDAR sorting junction to describe the microfluidic sorting process. When a cell is detected at the upper LIF detection line (**c**), the avalanche photodiode (APD) detects a peak in signal intensity (shown at right). This event triggers actuation of a solenoid positioned in line with buffer line 2, causing the flow to increase from the right and the stream of blood to move to the left outlet (**d**), creating an aliquot of blood with the cell of interest. The solenoid then turns off and flow returns to normal (**e**) Finally, the aliquot passes by a second LIF detection line (the lower line) to confirm the sort.

Previously, our group developed a highly sensitive CTC detection platform called eDAR, which stands for ensemble decision aliquot ranking. eDAR has been shown to be a robust platform for whole-blood isolation of rare cells present at levels as low as 1-10 cells/ml.<sup>28</sup> The platform uses laser-induced fluorescent (LIF) detection and microfluidic sorting of CTC-containing nanoliter-scale aliquots of whole blood (Figure 2.1).<sup>28</sup> In a side-by-side comparison with a commercial CTC-detection platform, CellSearch<sup>TM</sup>, eDAR detected CTCs in 82 out of 90 blood samples from stage IV breast cancer patients while CellSearch<sup>TM</sup> detected CTCs in only 40 out of 90 samples.<sup>29</sup> Recoveries of spiked-in MCF-7 cells were 95%, with spike-in numbers between 10 to 100 cells per sample.<sup>7</sup>

In this paper, we targeted the detection and isolation of CTCs that express low levels of the target antigen epithelial cell adhesion marker, EpCAM, by combining eDAR with an enhanced immunofluorescence labeling strategy. Specifically, we used a cocktail of CTC-specific primary antibodies targeting both mesenchymal and epithelial cell surface markers as well as a single dye-linked secondary antibody. We demonstrated the detection of CTCs that otherwise would be missed by targeting EpCAM alone with a dye-linked primary antibody. We quantified the improved detection with both a model cell line that expresses low levels of EpCAM (EpCAM<sup>low</sup>) spiked into whole blood and blood samples taken from breast cancer patients. The immunolabeling strategy is an important improvement over our previously published results as it addresses the heterogeneous nature of CTCs that makes them difficult to detect. The strategy also expands the limit of detection (LOD) in a quantifiable manner, which is important for accurate CTC counts in patient samples. There are two advantages of our two-step labeling strategy with more than one antibody: 1) The dye brightness from all of the targeted CTC markers is additive without an increase in the background fluorescence signal, and 2) Our

chances of detecting CTCs are improved because any given CTC will robustly express at least one of the cell surface markers.

With our approach, we demonstrated an 86% recovery of cells from a model cell line and a 6-fold increase in the number of CTCs isolated from blood samples taken from three breast cancer patients. These results support the assertion that while EpCAM<sup>high</sup> cells provide a point of comparison between CTC isolation techniques, the recovery rates obtained are not necessarily representative of true CTC recovery rates, especially for patients with a significant proportion of EpCAM<sup>low</sup> CTCs.

## 2.3 METHODS

### 2.3.1 *Cell culture.*

MCF-7 and MDA-MB-231 cell lines were obtained from American Type Culture Collection (ATCC, Manassas, VA). Cell lines were cultured at 37 °C and 5% CO<sub>2</sub> in EMEM and DMEM media (ATCC), respectively. Media was supplemented with 5% v/v fetal bovine serum (FBS) and 1% v/v penicillin streptomycin (both from Sigma, St Louis, MO).

### 2.3.2 *Clinical samples.*

Healthy whole blood was obtained from PlasmaLab International (Everett, WA). The samples of peripheral blood from breast cancer patients were obtained from NWBioTrust (Seattle, WA), using a protocol approved by the University of Washington Internal Review Board. All blood samples were collected in BD Vacutainer EDTA tubes (Franklin Lakes, NJ). Blood was processed within two days of collection and stored at 4°C.

### 2.3.3 *Reagents.*

Antibodies were purchased from BioLegend, Inc. (San Diego, CA) with the exception of phycoerythrin (PE)-anti-EpCAM (Abcam, Cambridge, MA). Cell fixation buffer and permeabilization (saponin) buffer were obtained from BioLegend and Sigma, respectively. The saponin solution was made at 1% wt/wt in MilliQ water (EMD Millipore, Billerica, MA) and used at a final working concentration of 0.1%. Cell staining buffer for flow cytometry was purchased from BioLegend. Isoton II buffer, used as a sheath flow for eDAR, was purchased from Beckman Coulter (Brea, CA). PE-labeled calibration beads (BD Quantibrite™ PE beads) for flow cytometry were purchased from BD Biosciences (Franklin Lakes, NJ).

### 2.3.4 *Microfluidic chips.*

Silicon masters were made as described previously.<sup>3</sup> Briefly, silicon masters were made using standard photolithographic techniques including deep reactive ion etching to define the on-chip in-plane slit filter. Chips were made from PDMS in a 1:10 ratio of precursor to polymer base, fully cured, and sealed to a glass substrate immediately following exposure to O<sub>2</sub> plasma for one minute. If not used immediately, chips were covered and stored until use, but not longer than one week.

### 2.3.5 *Flow cytometry.*

For flow cytometry analysis,  $\sim 1 \times 10^6$  cells were labeled in 1-mL labeling buffer, made with 1× PBS, 3% FBS, and 0.1% NaN<sub>3</sub> (Sigma), with 0.1× of the manufacturer's recommended labeling concentration of antibodies. This concentration was determined to provide optimal cell labeling by a binding curve analysis (see Supporting Information, Figure 2.5). Cells were labeled for one hour and then washed in 4-mL labeling buffer. Each of the washed cell-sample pellets

and the PE calibration beads were separately resuspended in 1-mL labeling buffer each immediately prior to flow cytometry analysis. Isotype controls were performed in flow cytometry to confirm specificity of primary antibody binding (see Supporting Information, Figure 2.6). FACS Scan and LSRII flow cytometers were used for all flow cytometry analysis at the University of Washington Cell Analysis facility. Data was analyzed using FlowJo (Ashford, OR) to obtain the geometric mean fluorescence intensity (FL2, 585/12 filter) of each cell population. A calibration curve obtained with the PE beads was used to convert these intensities to antibodies bound per cell (ABC).

### 2.3.6 *eDAR detection of spiked-in cultured cells.*

Approximately 200,000 cells were pipetted into 100- $\mu$ L Isoton. Next, 1 mL of whole blood was pipetted on top of the Isoton. Finally, 0.1 $\times$  of the recommended concentration of each antibody was added to the blood and incubated in the dark, at room temperature (21  $^{\circ}$ C) on a rocker for 1 hour. After incubation, samples were washed with 12-mL Isoton and centrifuged at 890 RCF for 10 min. The supernatant was removed to the original 1 ml volume carefully, so as not to disturb the cells. For the two-step labeling scheme, the secondary antibody (0.1 $\times$  recommended concentration) was added to the washed blood at this time. The incubation and washing steps were repeated. After completion of labeling, samples were processed within 2 hours. Using a syringe pump, samples were introduced into the sample inlet of the eDAR chip at a flow rate of 50  $\mu$ L/min and a fluorescence intensity trace from avalanche photodiodes (APDs) was collected for at least 5 min to obtain 50,000 data points. Excitation of the fluorescently labeled cells was achieved using a 488-nm laser. The resulting epi-fluorescence signal was divided into red, green, and yellow components and collected at APDs. The signal from the yellow channel was analyzed using MATLAB to obtain histograms of the fluorescence

intensities of the population of labeled cells. Antigen expression levels of these cells were determined by analyzing paired cell samples in flow cytometry with calibration beads. We found calibration in flow cytometry to be more accurate in determining antigen expression level on spiked-in cells than using the calibration beads in the eDAR chip. Using this method, we were able to analyze the eDAR response (fluorescence intensity peak area) in terms of PE-labeled antibodies bound for each cell population. By plotting the geometric mean intensities in eDAR versus those found in flow cytometry for several cell populations, we obtained a limit of detection (LOD) for eDAR of 5800 PE-labeled ABC (Antibody Bound per Cell). More details about the data analysis can be found in the Supplemental Information.

### *2.3.7 eDAR isolation of CTCs from patient-derived samples.*

To verify the hypothesis that the enhanced labeling scheme yielded higher recovery rates of CTCs, we analyzed paired blood samples, one labeled with PE-anti-EpCAM alone and one labeled with the cocktail scheme. The breast cancer samples we obtained for our study were classified based on the primary tumor expression of estrogen receptor (ER), progesterone receptor (PR) and human epidermal growth factor receptor 2 (HER2), as well the stage of the cancer (1-4). The three patients were classified as follows: patient 1 was stage 3, ER+ PR+ HER2-; patient 2 was stage 4, ER+ PR- HER2+; patient 3 was stage 2, ER+ PR+ HER2-; and patient 4 was stage 2, ER+PR+HER2-. The labeling process and eDAR recovery of CTCs followed previously reported protocols<sup>7</sup>. Briefly, 2 ml of whole blood was labeled with fluorescently-labeled antibodies for 1 hour and washed with 12 ml Isoton. The sample was then centrifuged at 890 RCF for 10 min and the supernatant removed to obtain the original 2 ml volume. Once fully labeled, blood was loaded into a syringe, and introduced into an eDAR chip (Figure 2.1a) at 50  $\mu$ l/min. Sorting was established by adjusting the sheath flow pressures until

blood flowed to the Waste 2 reservoir when an in-line solenoid was closed and to the filter when it was open (Figure 2.1 c-e). Aliquots of blood were sorted based on the presence or absence of a fluorescence signal when passing a laser-induced fluorescence (LIF) detection line, with positive aliquots going to a microfluidic filter with 5  $\mu\text{m}$  slits for further analysis and negative aliquots being sent to Waste 2. In the one-step EpCAM scheme, blood was labeled with PE-anti-EpCAM for 1 hour. In the two-step scheme, first, a cocktail of primary antibodies comprised of bare mouse-anti-human EpCAM, EGFR, HER2, and N-cadherin was added to the blood and labeled for 1 hour. After a washing step, the sample was labeled with the secondary antibody, PE-goat-anti-mouse-IgG, for 1 hour. The sample was washed again prior to being processed on eDAR. Blood from breast cancer patients was analyzed by eDAR within two days of being drawn.

After the whole volume of blood was sorted by eDAR, post-sorting labeling of the captured cells was carried out. Fixation and permeabilization buffers as well as the dye-linked antibodies were introduced to the capture area (slit filter) using a peristaltic pump (MiniPump, Variable Flow, Fisher). In this process, the fixation solution was flowed onto the chip, incubated for 10 minutes, and rinsed. Then, permeabilization buffer along with Alexa647-anti-pancytokeratin, DAPI (nuclear stain), and Alexa700-anti-CD45 (all from BioLegend) are flowed onto the on-chip filter and incubated for 30 min. Images were taken using a CCD camera (Model GC1380, Allied Vision, Exton, PA). The imaged cells were evaluated for CTC characteristics. The criteria for CTC identification were that the cells were EGFR<sup>+</sup>, HER2<sup>+</sup>, N-cadherin<sup>+</sup>, EpCAM<sup>+</sup>, or cytokeratin<sup>+</sup>, and CD45<sup>-</sup> with positive nuclear stain.

## 2.4 RESULTS AND DISCUSSION

### 2.4.1 *eDAR detection of a model EpCAM<sup>low</sup> cell line.*

A population of CTCs can have widely varied phenotypic characteristics because of the changes CTCs undergo as they escape from solid tumor tissue and enter the bloodstream. Most notably, CTCs from tumors of epithelial origin shed their epithelial phenotypic traits to differing degrees and assume mesenchymal hallmarks (a phenomenon known as EMT). Therefore, researchers can anticipate a wide distribution of expression levels for epithelial biomarkers, including the most common antigen targeted for CTC detection – EpCAM. Despite the variability in EpCAM expression, the prevailing method for benchmarking CTC isolation techniques is to spike EpCAM<sup>high</sup> cultured cancer cells, typically MCF-7 or SKBr3 for breast-cancer, into a sample of healthy blood. This approach provides inadequate information to determine the dependence of each technique's performance on the target cells' expression level of EpCAM. Cells that have undergone the EMT (and are therefore EpCAM<sup>low</sup>) are known to be more capable of survival in the bloodstream and more invasive. Therefore, it is critical to characterize the ability of a technique to isolate EpCAM<sup>low</sup> cells.

To demonstrate the impact of heterogeneity in EpCAM expression on CTC detection, we benchmarked eDAR performance using two cell lines with known EpCAM expression levels—MDA-MB-231 (EpCAM<sup>low</sup>) and MCF-7 (EpCAM<sup>high</sup>). The MDA-MB-231 cell line expresses approximately 10,000-15,000 EpCAM/cell and the MCF-7 cell line expresses approximately 100,000-500,000 EpCAM/cell based on flow cytometry analysis (three trials separated by several weeks). Previously, we demonstrated greater than 95% recovery of MCF-7 cells spiked into whole blood.<sup>7</sup> To evaluate the performance of eDAR for detection of EpCAM<sup>low</sup> cells, approximately  $3.0 \times 10^4$  MDA-MB-231 cells were spiked into 1 mL of blood and labeled with

PE-anti-EpCAM. The entire volume of blood was flowed through the eDAR chip, and the resulting fluorescence intensity trace was analyzed using an in-house peak recognition algorithm in MATLAB to count the percentage of cells detected. This approach yielded a detection rate of ~20%, which indicates that the majority of the cells fell below the LOD of eDAR.

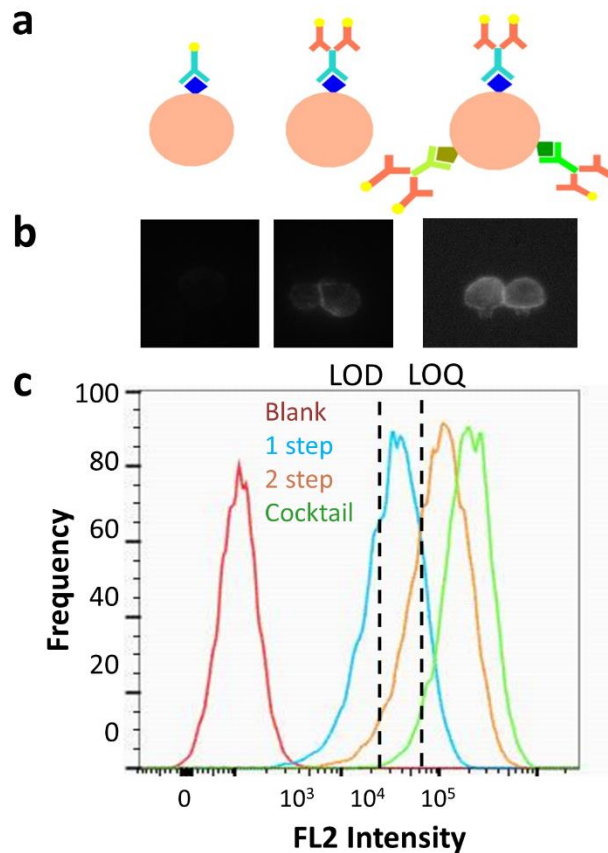


**Figure 2.2:** **a** Scheme of the three labeling strategies used: 1-step EpCAM, 2-step EpCAM, 2-step cocktail (from left to right). **b** Images of MDA-MB-231 cells labeled with each of the three strategies. **c** Flow cytometry histogram of the fluorescence intensities of MDA-MB-231 cells employing each of the three labeling strategies. The LOD (limit of detection) and LOQ (limit of quantification) of eDAR in terms of the number of PE molecules bound per cell are indicated by the dashed lines.

Initial progress towards detecting these EpCAM<sup>low</sup> cells was made by moving to a two-step scheme. This detection scheme consisted of a bare primary anti-EpCAM antibody followed by a PE-conjugated secondary antibody (Figure 2.2a and 2.2b). The strategy resulted in a 2- to 3-fold increase in brightness (Figure 2.2c) caused by multiple fluorescent secondary antibodies binding to each anti-EpCAM primary antibody. By this improvement alone, the detection rate for MDA-MB-231 cells increased to 60%. While nearly 85% of the cells were above the LOD of eDAR (Figure 2.2c), our threshold for sorting most practically was set at or slightly below the limit of quantitation ( $10\sigma$  above the average background, where  $\sigma$  is the standard deviation of the noise) due to fluctuations in the background fluorescence of the blood sample. Therefore, with the goal of capturing the majority of EpCAM<sup>low</sup> cells, we sought to further improve our labeling strategy.

To circumvent the limitations of the eDAR LIF detection scheme and to take advantage of the inherent brightness of PE-labeled antibodies, we decided to use a cocktail of antibodies all carrying the same fluorescent tag to generate an additive signal. This cocktail was designed to incorporate antibodies against both epithelial and mesenchymal markers to account for CTC heterogeneity. However, a cocktail of fluorescently-tagged primary antibodies yielded an unacceptable increase in background fluorescence in the blood. The problem arose from the post-labeling washing protocol: After mixing the labeled blood with Isoton buffer, the sample was centrifuged and the supernatant was pipetted off down to the original volume of whole blood (e.g. 1 mL). Therefore, there were residual unbound fluorescently-tagged antibodies in the retained fraction. We overcame this problem by using a cocktail of bare primary antibodies followed by a single dye-linked secondary antibody. With this approach, the fluorescence

background was only affected by the concentration of secondary antibody and was independent of the number of unique primary antibodies in the cocktail.

The antigens targeted by the cocktail were EpCAM, EGFR, HER2, and N-cadherin. EpCAM and EGFR are epithelial markers most often found on epithelial tumors. HER2 was included in anticipation of the analysis of clinical samples from breast cancer patients because HER2 is overexpressed in some types of breast cancer. We decided to use anti-HER2 labeling in all of our clinical samples (including those classified as HER2<sup>-</sup>) because there is evidence that even patients with HER2<sup>-</sup> status can have HER2<sup>+</sup> CTCs.<sup>30</sup> N-cadherin is a mesenchymal marker that has been noted in CTCs that have undergone the EMT.<sup>5</sup> Its inclusion in the cocktail was useful for the recovery of cells lacking epithelial characteristics.

The cocktail scheme was evaluated as follows. First,  $3.0 \times 10^4$  MDA-MB-231 cells were spiked into 1 mL of blood. Second, the blood was incubated for 1 hr with the cocktail of primary mouse-derived antibodies against EpCAM, EGFR, HER2, and N-cadherin and then washed. The sample was incubated for 1 hr with PE-goat-anti-mouse IgG and washed. Finally, the entire sample volume was flowed through the eDAR chip, and the resulting fluorescence intensity trace was analyzed. The detection rate of our approach was determined to be 86%.

Much of the observed improvement in detection rate was because the MDA-MB-231 cell line was EGFR positive. This result does not demonstrate enhanced detection of biomarkers that are underexpressed. However, the experiment illustrates the strength of the cocktail approach, which was further underscored by flow cytometry data (see SI Figure 2.7) that shows the intensity of MDA-MB-231 cells labeled for all biomarkers was the sum of that measured for each individual marker.

#### 2.4.2 *Quantitative approach to eDAR recovery efficiency.*

A significant advantage of eDAR over other CTC detection and isolation methods is that LIF detection lends itself to the quantification of targeted antigens. Other CTC isolation techniques can be limited in this regard; for example, when cells were captured by immunoaffinity binding of cells to an antibody-coated substrate,<sup>31</sup> a truly quantitative analysis of device performance versus antigen expression level would involve complex calculations that incorporate binding affinity, flow profiles, and cell characteristics. The only practical method for comparing CTC techniques to each other is to count the number of spiked-in cultured cancer cells recovered from a blood sample. MCF-7 (EpCAM<sup>high</sup>) cells are typically used. However, eDAR does not share in this limitation because the impact of antigen expression on capture efficiency can be independently quantified.

There are a number of steps in eDAR that contribute to the overall recovery rate of the system, with each step having a distinct probability for CTC loss. These steps include: 1) sample processing (labeling, washing, and transfer steps), 2) CTC detection by LIF, 3) CTC capture on the filter, and 4) confirmation by imaging. The probability of CTC loss is not easily described at all of these steps. However, we do know that for EpCAM<sup>high</sup> cells, the recovery efficiency averages 95%. We can assume when we work with cells with lower EpCAM expression levels that the losses from steps 1, 3, and 4 remain constant but the loss from step 2 (LIF detection) decreases with decreased cell brightness. Once the LIF detection is well characterized, separate spike-in and recovery experiments are not required to calculate recovery efficiency for new labeling schemes or cell types. Therefore, we can forecast the recovery efficiency for any cell population with a known distribution of antigen expression.

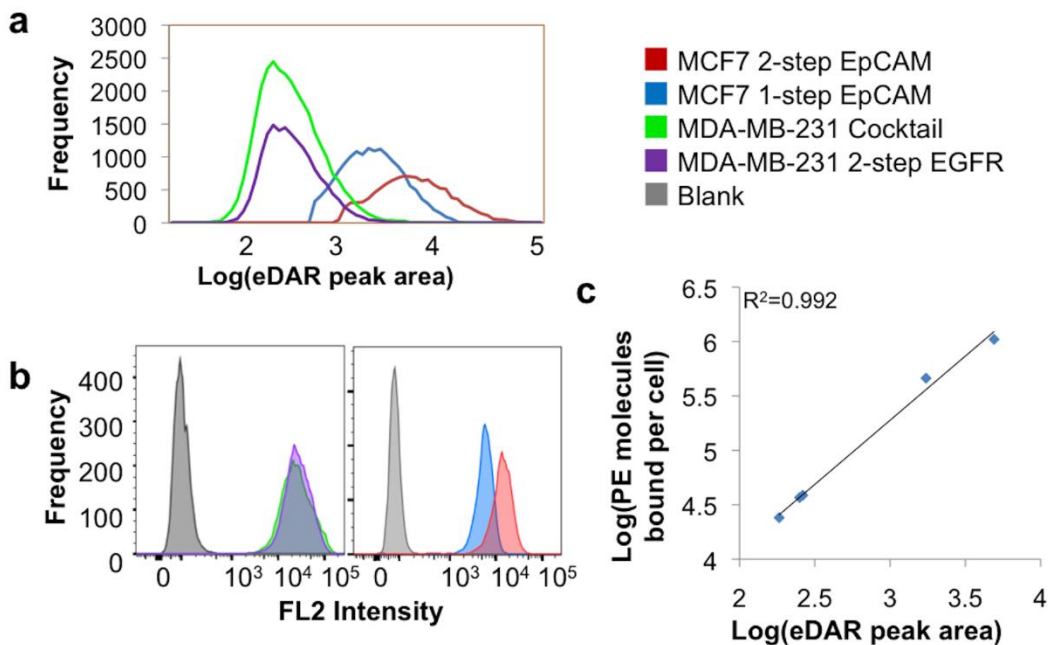


**Figure 2.3:** **a** Histogram showing the distribution of cell brightness from the four cell populations measured in eDAR. The four populations were labeled and spiked into blood for eDAR analysis or into buffer for flow cytometry analysis. **b** Flow cytometry histograms of the same four populations. **c** Plot of the geometric mean intensities of the four cell populations comparing the number of PE molecules bound to the peak area measured in eDAR. The high  $R^2$  value indicates that eDAR is quantitative with respect to antigen expression and that the modes from eDAR and flow cytometry can be used to determine the LOD.

A related advantage of the eDAR format is that it lends itself to spike-in studies with a statistically relevant number of cells (tens of thousands). Figure 2.3a shows histograms for four different cell populations derived from eDAR fluorescence intensity traces. The histograms were plotted using the log of peak area for each event on the trace going above a cutoff threshold (above  $6\sigma$ ). The four cell populations were comprised of two cell types, each processed by the two labeling schemes. These four eDAR samples were prepared as follows. First, each cell population was labeled in cell labeling buffer and subsequently divided into two portions (the

first portion for eDAR and the second for flow cytometry). For eDAR, a total of 30,000-40,000 cells from each population was spiked into four separate 1-mL blood samples and then flowed through the eDAR chip as the intensity trace was recorded. Importantly, these blood samples were pre-washed (before spiking in cells) to account for the processing that occurs during eDAR analysis of a clinical sample. Of these four populations, MDA-MB-231 cells labeled for EGFR by the 2-step scheme were the dimmest while the MCF-7 cells labeled for EpCAM by the 2-step scheme were the brightest. For the brightest population, a neutral density filter was required to bring the fluorescence intensity down into the linear range of the APD. To characterize the number of PE molecules bound to the cells, the remaining second portion of the labeled cells was analyzed by flow cytometry, and the intensity was translated to the number of PE-linked ABC using PE calibration beads (Figure 2.3b).

The results demonstrate that the eDAR peak area is a quantitative measure of the number of PE-linked ABC. Specifically, the cell populations yielded similar distributions by eDAR and flow cytometry; when plotted against each other, the geometric mean intensities from both techniques yielded a straight line (Figure 2.3c,  $R^2 = 0.992$ ). Using this data, we estimated for eDAR an LOD of 5,800 PE molecules per cell and a LOQ of 23,500 PE molecules per cell (see SI for discussion of LOD and LOQ determination). It should be noted that the LOQ is more relevant to CTC recovery rates than the LOD because under practical operating conditions, the sorting threshold for eDAR is usually set near the LOQ. As the fluorescence background from the blood sample fluctuates, sorting can be triggered in error, sending an excessive number of CTC-negative aliquots of blood to the filter. Defining an LOQ for eDAR is significant because it establishes a cut-off for CTC detection. An LOQ of 23,500 PE molecules/cell means that cells having 23,500 dye-linked ABC will be reliably detected and sorted.

Finally, the data underscore that eDAR is capable of providing quantitative data for biomarker expression levels falling within the linear range of detected intensities. While the current linear range of eDAR does not extend to sufficiently high intensities to quantify antigen expression on EpCAM<sup>high</sup> cells labeled using the 2-step scheme, the range can be extended to higher intensities simply by splitting off 1% of the signal to a separate APD. For many CTC technologies, quantitative data is not obtained during the capture step. Some techniques, such as CellSearch, exploit EpCAM as a binding site for magnetically-tagged antibodies and block these sites from further analysis.<sup>15</sup> Other techniques allow for downstream quantification of EpCAM during post-secondary labeling and imaging steps. However, post-secondary quantification of EpCAM is time-consuming. eDAR's ability to provide rapid quantitative measurements is significant because the expression level of EpCAM (or other biomarkers) on CTCs may prove to be clinically relevant.

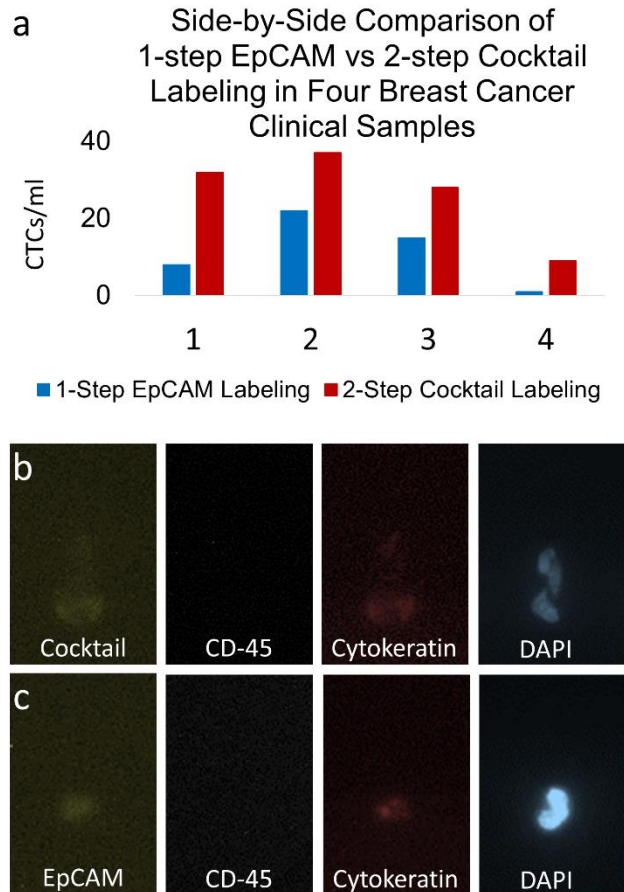


**Figure 2.4:** Cells from breast cancer clinical samples were sorted on an eDAR chip. Following sorting, the cells were fixed, permeabilized and labeled with CD45-alexa700, Pancytokeratin-alexa647 and DAPI to verify whether the cells were CTCs. **a** Chart showing the number of CTCs recovered from each of four clinical breast samples, where 2 ml of blood was run with each 1-step EpCAM and 2-step cocktail. Patient 1 was stage 3, ER/PR+HER2-, patient 2 was stage 4, ER+PR-HER2+, patient 3 was stage 2, ER/PR+HER2- and patient 4 was stage 2, ER+PR+HER2-. **b.** Fluorescence images of a cell captured by eDAR using the cocktail labeling scheme (Cocktail included primary bare anti-EpCAM, anti-EGFR, anti-HER2, and anti-N-Cadherin followed by secondary PE-goat-anti-mouse-IgG). **c** A cell detected using the 1-step PE-anti-EpCAM labeling scheme.

### 2.4.3 *6-fold increased recovery of CTCs from patient-derived samples.*

The relevance and success of the cocktail labeling scheme that we developed needed to be evaluated with clinical samples. To quantify the improvement, we compared the cocktail labeling scheme to our former labeling strategy of PE-anti-EpCAM alone. Figure 2.4a shows a bar graph with the number of CTCs isolated with each labeling scheme (cocktail and PE-anti-EpCAM) for each of the samples obtained from four breast cancer patients. Patient 1 was stage 3, ER+ PR+ HER2-; patient 2 was stage 4, ER+ PR- HER2+; patient 3 was stage 2, ER+ PR+ HER2-; and patient 4 was stage 2, ER+PR+HER2-.. In this experiment, each sample was divided into two 2-mL portions. The samples were analyzed by eDAR sequentially using each of the two labeling schemes. Samples were processed within two days after the blood was drawn. The data in Figure 2.4a demonstrate that a significant improvement, averaging 6×, was observed with the cocktail scheme. Figure 2.4b and c show representative cells that were isolated and further labeled against CD45, cytokeratin, and DAPI (post-capture) to confirm CTC identity.

These results demonstrate a significant improvement in CTC recovery with our cocktail labeling scheme. They also validate the assertion that there are EpCAM<sup>low</sup> CTCs in the blood of breast cancer patients. We increased the capability to isolate and characterize these EpCAM<sup>low</sup> cells that represent a potentially more invasive population of CTCs. This enhanced sensitivity and selectivity can take advantage of our dual-filter sorting chip to isolate two distinct cell populations (high and low EpCAM expression) to separate on-chip filters.<sup>32</sup> Finally, we are in the process of developing downstream analytical tools to extract genetic and phenotypic information from the CTCs. The information will be critical in unraveling the mechanisms of metastasis and developing anti-metastatic drugs.

## 2.5 CONCLUSION

We demonstrated the improved detection of CTCs in whole blood with a cocktail labeling scheme targeted against both epithelial and mesenchymal biomarkers. We validated the approach first with a model EpCAM<sup>low</sup> cell line and then with samples taken from breast cancer patients. Detection rates for EpCAM<sup>low</sup> cells were improved from 20% with our earlier eDAR protocol to 86%. More significantly, the number of CTCs recovered from the clinical samples was increased 6-fold. This improvement is particularly important in light of a growing body of research demonstrating both the prevalence and invasiveness of EpCAM<sup>low</sup> CTCs.

We further demonstrated two distinct advantages of eDAR including: 1) ability to establish LOD and LOQ values for dye-linked ABC and antigen expression level, and 2) quantitative data about CTCs' surface antigen expression levels during the detection step. Many CTC detection schemes are benchmarked solely based of recovered cells from spike-in samples. However, the most common cell line used in CTC technology development, MCF-7, expresses high levels of EpCAM, which is unlikely to represent all CTCs found in cancer patients. The ability to detect, isolate and analyze the full spectrum of CTCs, including the frequently missed EpCAM<sup>low</sup> cells, from patient samples poises eDAR for both improved cancer diagnostics and deeper study of cancer metastasis. Most significantly, eDAR may enable us to uncover the correlations between antigen expression and disease outcomes.

## 2.6 SUPPORTING INFORMATION

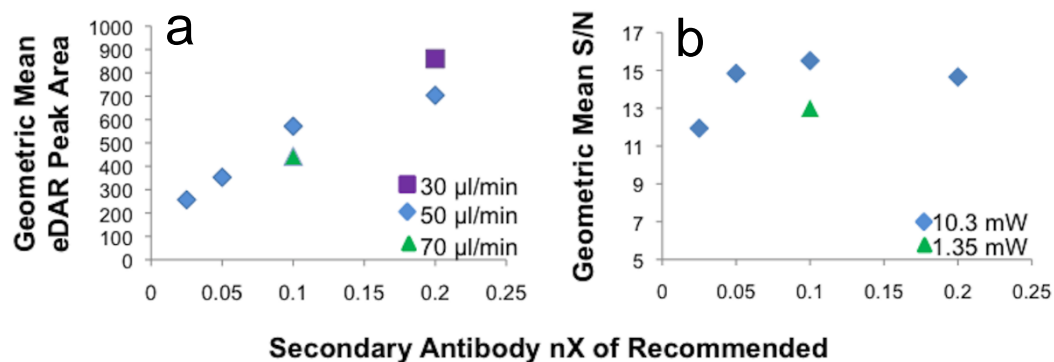


**Figure 2.5** Plots demonstrating the impact of the concentration of dye-linked secondary antibody on the detection of the labeled cells in eDAR. a) Geometric mean eDAR peak area versus secondary antibody concentration. b) Geometric mean peak intensity divided by the standard deviation of the background intensity (S/N ratio) plotted against secondary antibody concentration.

### 2.6.1 Parametric evaluation of measured signal intensity and signal-to-noise ratio in eDAR.

To determine optimal conditions for eDAR, we conducted a parametric study (Figure 2.5), in which we independently varied the antibody concentration, laser power, and flow rate. All other conditions were held constant and were consistent with those described in the Experimental Section of the main text. To determine the optimal antibody labeling conditions, we labeled separate populations of MDA-MB-231 cells with a range of concentrations (0.025 $\times$  to 0.25 $\times$  the recommended concentration of  $\leq 0.5 \mu\text{g}$  per  $1 \times 10^6$  cells in  $100 \mu\text{L}$  solution) of the secondary antibody (PE-goat-anti-mouse IgG). Then we chose the lowest dye concentration that could achieve an acceptable labeling intensity. Figure 2.5a shows the resulting geometric mean eDAR peak areas achieved for each population of cells. We determined that the geometric mean

peak area achieved with 0.1× of the recommended dye-linked antibody concentration was acceptable. Furthermore, from the same data set, we plotted the geometric mean signal-to-noise ratio (the geometric mean eDAR peak intensity divided by the standard deviation of the background). The result, shown in Figure 2.5b, demonstrates that 0.1× of the primary antibody provided the highest geometric mean background subtracted eDAR intensity. In these two plots, we have indicated the impact of sample flow rate (Figure 2.5a) and laser intensity (Figure 2.5b). Figure 2.5a demonstrates the impact of flow rate on the geometric mean eDAR peak area. For the two highest dye-linked antibody concentrations, we varied the sample flow rate from 50  $\mu\text{L}/\text{min}$  to 30  $\mu\text{L}/\text{min}$  and 70  $\mu\text{L}/\text{min}$ . We concluded that a slower flow rate yielded a higher eDAR peak area. We determined that the sample flow rate presents a trade-off between signal and sample throughput, and we ran all subsequent experiments at 50  $\mu\text{L}/\text{min}$ . Figure 2.5b shows the impact of the laser intensity on the S/N. The results show that a laser power of 10.3 mW yielded ~20% greater S/N than a 1.35-mW laser power. We determined that 10.3 mW provided improved detection of the most dimly labeled cells (MDA-MB-231) but caused the signal for the most brightly labeled cells (MCF-7) to exceed the quantitative range of eDAR ('max out' the detector). With the goal of detecting model cell lines and CTCs with low expression of targeted antigens, we decided to use a laser power of 10.3 mW for all of our subsequent experiments.

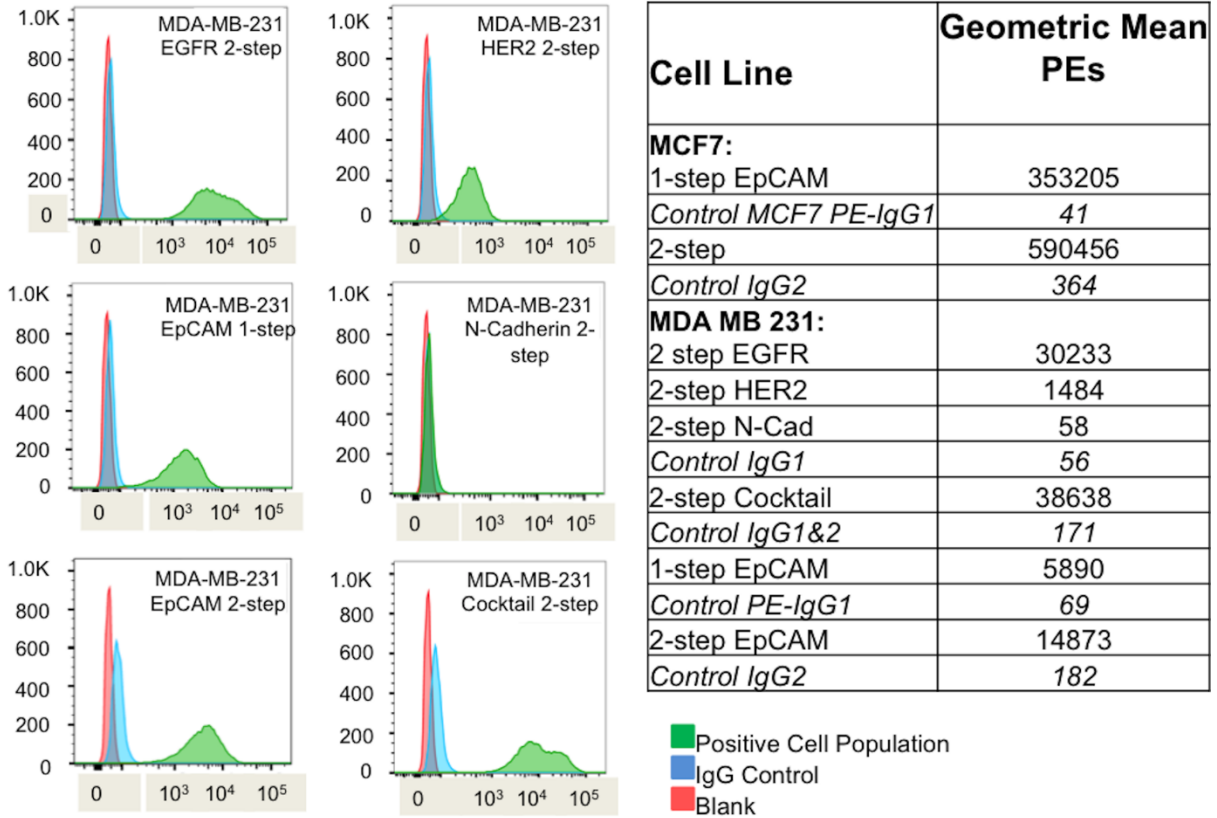


**Figure 2.6** Isotype control experiments. Separate populations of MDA-MB-231 cells were labeled with each primary antibody (EpCAM, HER2, EGFR, N-cadherin) and the corresponding IgG antibody followed by the secondary antibody to verify specificity of primary antibody labeling.

### 2.6.2 Isotype control experiments.

To test the specificity of the primary antibodies, we ran a series of isotype controls. The cells were labeled as described in the main text with the exception that the appropriate IgG control replaced the primary antibody. The IgG control antibody was selected based on the recommendation of the supplier. For 1-step labeling procedures, a dye-linked IgG control antibody was used; for the 2-step labeling procedures, a bare primary IgG control antibody was

followed by a dye-linked secondary antibody. Figure 2.6 shows the results of these trials, with the geometric mean number of dye-linked antibodies bound per cell (ABC) shown on the right. These ABC values were calculated using the same PE calibration beads we used in the calibration of eDAR (see main text).

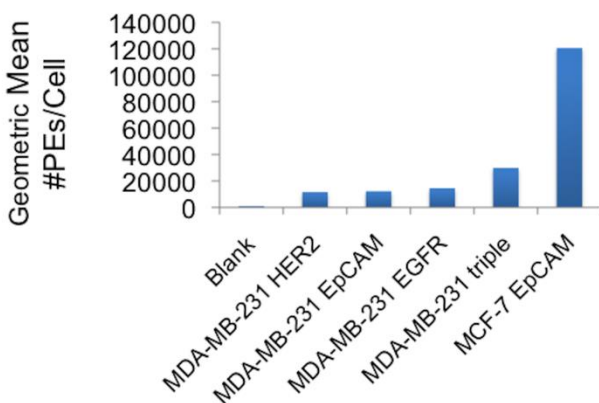


**Figure 2.7** MDA-MB-231 cells labeled with three antibodies (EpCAM, HER2, EGFR) and a cocktail of all three, demonstrating that the antibody brightness is additive.

### 2.6.3 eDAR calibration.

We calibrated eDAR with a variety of cell types and labeling strategies within the dynamic range of eDAR and flow cytometry. The geometric mean number of PE dye molecules bound per cell for each population was determined against PE calibration beads in flow cytometry. The beads had four distinct populations with a known number of PEs that could be correlated to the cells run on the same instrument. Using the geometric mean intensities calculated in FlowJo, we determined the number of PE molecules bound per cell population. Then, on the same day, we ran a subset of each of the same labeled cell populations on eDAR and correlated the geometric mean eDAR peak area with PE molecules bound per cell. The data from eDAR is limited past a response of about 1500 intensity units (3.2 on a log scale) based the

maximum signal of the avalanche photodiode (APD) used for detection. However, eDAR dynamic range can be extended into brighter cells with ND filters which remove a known portion of the light but can be added back in for data analysis. It is important to note that the high end of the eDAR range is not a limit to the detection of bright cells, since a response of 1500 intensity units is more than sufficient to trigger sorting. It only works as a limiting factor in calibrating the system, which can be compensated for with ND filters.

To calculate the limit of detection (LOD) in terms of the number of PE molecules bound per cell ( $LOD_{\#PEs}$ ), we calculated the eDAR peak area that would be required to generate a peak height reaching the LOD in terms of intensity ( $3\sigma$  of background noise). This calculation accounted for the average peak shape, as determined using MATLAB. The LOD we found was 5800 PE molecules bound per cell and the LOQ was 23,500 PE molecules bound per cell.

Chapter 3.

NEGATIVE DIELECTROPHORETIC CAPTURE  
AND REPULSION OF SINGLE CELLS AT A  
BIPOLAR ELECTRODE: THE IMPACT OF  
FARADAIC ION ENRICHMENT AND  
DEPLETION

Reprinted with permission from “Anand, R. K.; Johnson, E. S.; Chiu, D. T. *J. Am. Chem. Soc.* **2015**, *137* (2), 776–783” Copyright 2015 American Chemical Society

### 3.1 ABSTRACT

This paper describes the dielectrophoretic (DEP) forces generated by a bipolar electrode (BPE) in a microfluidic device and elucidates the impact of faradaic ion enrichment and depletion (FIE and FID) on electric field gradients. DEP technologies for manipulating biological cells provide several distinct advantages over other cell-handling techniques including label-free selectivity, inexpensive device components, and amenability to single-cell and array-based applications. However, extension to the array format is nontrivial, and DEP forces are notoriously short-range, limiting device dimensions and throughput. BPEs present an attractive option for DEP because of the ease with which they can be arrayed. Here, we present experimental results demonstrating both negative DEP (nDEP) attraction and repulsion of B-cells from each a BPE cathode and anode. The direction of nDEP force in each case was determined by whether the conditions for FIE or FID were chosen in the experimental design. We conclude that FIE and FID zones generated by BPEs can be exploited to shape and extend the electric field gradients that are responsible for DEP force.

### 3.2 INTRODUCTION

We present a dielectrophoresis (DEP) technique that employs electric field gradients formed by localized faradaic ion enrichment and depletion (FIE and FID) zones at bipolar electrodes (BPEs) in a microfluidic device for the manipulation of a few or single cells. This technological development is significant because (1) it addresses a need for effective and

inexpensive single-cell manipulation in microfluidic devices, (2) the FIE and FID zones provide electric field gradients having a tunable size and shape, and (3) the use of BPEs allows facile arraying.

Over the past decade, the scientific community has become increasingly attuned to heterogeneity in seemingly homogeneous cell populations. Even among clonal cells, stochastic events lead to variations in gene expression and diverse responses to endogenous and exogenous stimuli. Cellular heterogeneity has documented impact in many fields of research such as the rare induction of somatic cells into pluripotent stem cells,<sup>33</sup> division of labor in neighboring neurons,<sup>34</sup> and varied drug response.<sup>35</sup> Heterogeneity within cancer cell populations<sup>36,37</sup> is of special interest for cancer treatment strategies because a minority of drug resistant cells can seed cancer recurrence after ‘clinical cure.’ None of these processes can be studied effectively using ensemble measurements, and therefore, many highly sensitive analytical tools have been developed for probing single cells.<sup>38,39</sup>

An ongoing challenge in single-cell analysis is manipulation (e.g., transport, sorting, trapping, and filtering) of the cells of interest. DEP manipulation of cells has been used to accomplish all of these functions while maintaining a high degree of cell viability. DEP is especially attractive for several reasons. First, cells can often be distinguished without the addition of labels (e.g., magnetic particles or fluorophores) owing to polarizabilities unique to cellular phenotype, size, and viability.<sup>40-43</sup> Second, DEP devices are generally comprised of planar electrodes or insulating barriers made of sufficiently inexpensive components to allow the production of disposable devices, an especially desirable characteristic for medical diagnostics devices, for which cross-contamination must be avoided.<sup>42</sup> Third, DEP has been demonstrated to be useful for single cell manipulation.<sup>44-46</sup> This has been accomplished by constraining the

trapping point either by adding physical barriers or by defining an electric field cage similar in size to a single cell. In either case, DEP conditions are chosen that prevent cell–cell attraction, thus discouraging multicell capture. Finally, DEP can be more easily operated in parallel versus some competing technologies such as optical tweezers<sup>38</sup> or purely fluidic systems, which require a network of pumps and valves.<sup>38,47</sup>

Despite these major advantages, current DEP technologies have remaining challenges to overcome, and three of the most serious shortcomings relate to the generation of the electric field gradient required for DEP force. First, while DEP technologies can be operated in parallel, there are practical barriers to achieving an array of local electric field gradients. There are two common ways of forming gradients in an applied electric field—namely, (1) by applying a nonuniform field with closely spaced electrodes and (2) by constraining the field with insulating barriers. Devices that form electric field gradients based on electrode arrays require the fabrication and actuation of many electrodes and wire leads—thereby leading to complex design and external instrumental control. Devices comprised of insulating barriers can only achieve precise trapping locations in positive DEP operating conditions, in which cells are trapped at vertices or constrictions where electric field maxima may be damaging to the cells. Second, the range over which DEP force exists around these electrodes and insulating barriers can be too short for high-throughput device operation.<sup>42,48</sup> Specifically, significant field gradients are often effective over one to several cell diameters. This problem has been partially addressed by complex device fabrication techniques that implement 3D electrodes, including modification of microfluidic channel walls and ceiling.<sup>42</sup>

Third and finally, the shape of the electric field gradient produced by each of these strategies is fixed, lacking plasticity. One recently developed technology, optical DEP (or

optoelectronic tweezers, OETs), has addressed this shortcoming through real-time light-based patterning of “virtual electrodes” in a semiconducting layer under a DEP chamber.<sup>49,50</sup> While OETs offer unprecedented spatial control over DEP force, the integration of OET materials and structures with existing microfluidic modalities is nontrivial.

Here, we employ BPEs to exert DEP force, and we modulate this force via the local conductivity of an aqueous medium.<sup>51–55</sup> This technique differs from medium conductivity gradient DEP, used to sort particles based on their conductivities,<sup>56</sup> in that, here, steeper gradients are locally and electrochemically generated, thus enabling them to contribute significantly to the DEP force experienced by cells near the BPE. As a result, cells are trapped or repelled by the resulting electric field gradients. Importantly, this technology addresses each of the challenges faced by existing DEP technology. First, BPEs can be operated in an array format without requiring wire leads (electrical contact) to each individual BPE.<sup>57</sup> As a result, the device is simple to fabricate. Second, the electric field gradients, which exert DEP force on the cells, have controllable size and can traverse the microchannel cross section. This feature is important because the device dimensions and throughput are not limited by short-range DEP forces. Finally, the shape of the electric field gradient can be tuned fluidically. In the following sections we describe the operating principles of the DEP at a BPE and describe initial results demonstrating the manipulation of cells.

### 3.3 THEORETICAL BACKGROUND

### 3.3.1 Bipolar Electrochemistry

Figure 3.1 is an illustration of a bipolar electrode (BPE)—here, a planar strip of conducting material—in a microfluidic channel. When a DC voltage bias is applied across the fluidic channel, a linear potential profile develops (solid line, Figure

3.1b). The potential of the BPE ( $U_{\text{BPE}}$ ) floats to a value intermediate to the potential of the aqueous solution in contact with its ends. The potential difference ( $\eta$ ) between the BPE and solution is a driving force for oxidation ( $\eta_{\text{a}}$ ) and reduction ( $\eta_{\text{c}}$ ) reactions at opposite ends of the BPE. Importantly, faradaic reactions are achieved at the BPE without direct electrical contact to the BPE, and this feature allows multiple BPEs to be operated in parallel. The rates of electron transfer to (oxidation) and from (reduction) the BPE are coupled and lead to a current through the BPE ( $i_{\text{BPE}}$ ).<sup>58</sup> Note that when  $i_{\text{BPE}}$  is nonzero, it competes with ionic current in the microchannel and impacts the potential drop in solution as indicated by the dashed line in Figure 3.1b.<sup>59</sup>

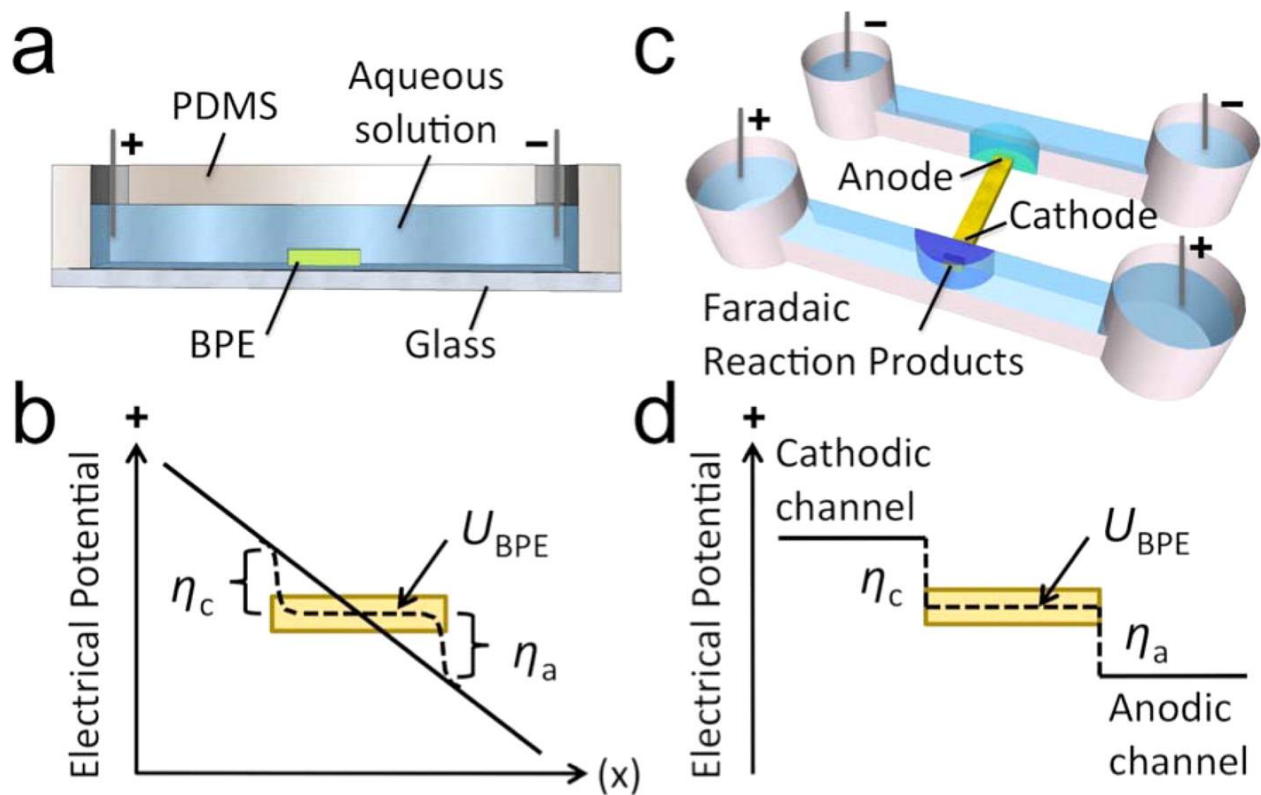
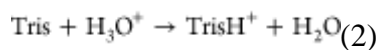
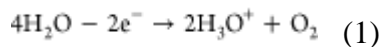


**Figure 3.1.** Microfluidic Devices Comprising a Bipolar Electrode and Illustration of Overpotential ( $\eta$ )

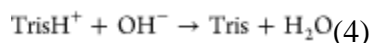
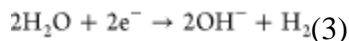
### 3.3.2 Generation of Faradaic Ion Enrichment and Depletion (FIE and FID) Zones

Faradaic electrochemistry at the BPE ends can perturb the electric field through the formation of FIE (high conductivity, low field strength) or FID (low conductivity, high field strength) zones. For example, an increase in local ionic strength at the anodic end of a BPE has been demonstrated to occur via water oxidation followed by Tris buffer protonation.<sup>51</sup>



Within the confinement of a microfluidic channel, this increased concentration of  $\text{TrisH}^+$  cations can remain localized around the anodic end of the BPE. Anions will electromigrate to charge pair

with these cations, forming an FIE zone.<sup>51</sup> Importantly, any oxidation or reduction reaction adding charge to a solution-phase species can similarly lead to an accumulation of positively and negatively charged ions at *either* the BPE anode or cathode. Conversely, a decrease in local ionic strength at the cathodic end of a BPE has been demonstrated to occur via the following set of reactions.<sup>51</sup>



The net result of this series of reactions is the neutralization of the buffer cation,  $\text{TrisH}^+$  to neutral Tris. In this case, the coanion ( $\text{Cl}^-$ ) was shown to migrate away from the site of neutralization, thus leading to localized FID at the BPE cathode.<sup>51</sup> Likewise, the neutralization of any charged species can lead to formation of an FID zone. Importantly, the shape and position of the FIE and FID zones can be controlled using convection.<sup>53</sup>

Finally, these FIE and FID zones have been formed at BPE ends that are fluidically isolated as shown in Figure 3.1c. In this case, the solution potential in contact with the BPE in the cathodic channel is higher than  $U_{\text{BPE}}$  and, in the anodic channel, is lower than  $U_{\text{BPE}}$  (Figure 3.1d). Note that the solution potentials represented in figure 3.1d are for the solution directly above the BPE and do not represent the potential profile along the length of each microchannel. A key advantage of this device configuration is that the applied DC voltage required to drive faradaic processes is significantly lower than the case in the single channel design. This improvement is owed to the removal of an ionic current path (fluidic junction) between the anodic and cathodic driving electrodes. This dual channel system has been used for electrophoretic enrichment of charged species<sup>51-55</sup> and electrostatic repulsion-based desalination<sup>60</sup> in DC-only electric fields.

### 3.3.3 DEP Manipulation of Cells Using BPEs

Here, we utilize these FIE and FID zones for DEP attraction and repulsion of biological cells. The mechanism by which ion concentration impacts DEP force is described here briefly. A polarizable particle subjected to an electric field will develop an effective dipole moment,  $p$  (Figure 3.2a).<sup>41</sup> The magnitude of the dipole depends upon the volume of the particle, its degree of polarizability, and the strength of the surrounding electric field ( $E$ ). In the presence of an electric field gradient, the particle will be attracted to regions of higher  $|E|$  if the complex permittivity of the particle ( $\epsilon^*_p$ ) is greater than the complex permittivity of the surrounding medium ( $\epsilon^*_m$ ). This condition is called positive DEP (pDEP). Conversely, negative DEP (nDEP) will occur if  $\epsilon^*_p$  is less than  $\epsilon^*_m$ . The magnitude of DEP force ( $F_{DEP}$ ) exerted on a spherical particle is given by the following equation

$$F_{DEP} = 2\pi r^3 \epsilon_m \text{Re}[K(\omega)] \nabla |E_{RMS}|^2 \quad (5)$$

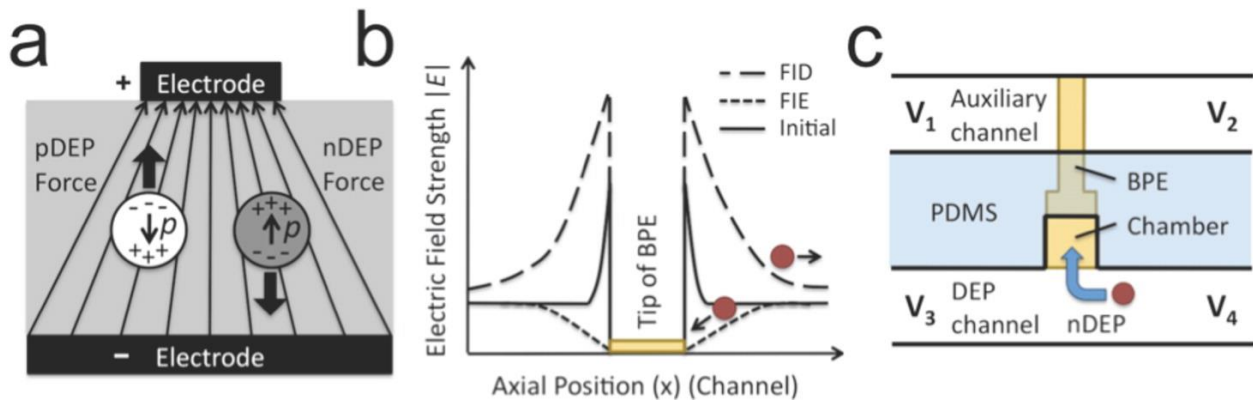


**Figure 3.2** Principles of nDEP Repulsion and Capture at FID and FIE Zones near a BPE Tip

Here,  $r$  is the particle radius and  $\text{Re}[K(\omega)]$  is the real part of the Clausius–Mossotti factor ( $K$ ), which is a function of electric field frequency ( $\omega$ )

$$K = (\epsilon_p^* - \epsilon_m^*) / (\epsilon_p^* + 2\epsilon_m^*) \quad (6)$$

$$\epsilon^* = \epsilon + \frac{i\sigma}{\omega} \quad (7)$$

Equations 5–7 highlight the dramatic impact that a local change in solution conductivity ( $\sigma$ ) can have on  $F_{\text{DEP}}$ . Specifically, the formation of an FID zone leads to an ohmic increase in the local magnitude of  $E$  and, simultaneously, causes  $\epsilon_m^*$  to decrease (making  $K$  more positive). Likewise, FIE can have the opposite effect on  $E$  and  $\epsilon_m^*$ . This synergistic effect is important because, as a particle is attracted (for instance, by pDEP into a high  $|E|$  region), the magnitude of  $K$  can increase, leading to amplified attraction.

The experimental results presented here demonstrate nDEP attraction and repulsion of B-cells to and from FIE and FID zones generated at a BPE in a microfluidic device. These conductivity gradients act as extensions to the BPE, thus impacting a larger volume than the electric field gradients surrounding a typical planar electrode. Figure 3.2b (not to scale) illustrates the anticipated impact of FIE and FID on the axial component of the electric field adjacent to *either end* of a BPE in a microfluidic device (such as that depicted in Figure 3.1c). This simplified depiction assumes that the driving voltage applied to the device is symmetrical about the BPE. At an active BPE (i.e.,  $i_{\text{BPE}} \neq 0$ ) the electric field is zero directly above the BPE and enhanced at the BPE edges (Figure 3.2b, solid line). The formation of an FIE zone leads to an ohmic decrease in the local magnitude of  $E$ , with the greatest impact nearest the BPE. At the BPE, the electric field remains zero. A cell will be trapped by nDEP at the resulting electric field minimum, at which the cell has a reduced risk of electric field-induced damage. Conversely, FID

leads to an increase in the local magnitude of  $E$ , leading to enhanced and extended nDEP repulsion of a cell from the BPE. Previous measurements and simulations of  $E$  have shown that an electric field gradient formed by FIE and FID can extend up to several hundred microns from the BPE.<sup>51,53,55</sup> Table 3.1 shows the estimated nDEP force experienced by 10  $\mu\text{m}$ - and 20  $\mu\text{m}$ -diameter cells at the field maxima of electric field gradients attainable by FIE and FID. As a point of reference, the drag force experienced by these cells moving through solution at 20  $\mu\text{m/s}$  is 1.9 and 3.8 pN, respectively. Although stronger fields may be used in certain applications, the maximum field strengths shown here are limited by the threshold of the transmembrane potential for electroporation (approximately 0.5 V).<sup>61</sup> The exact threshold at which electroporation occurs is determined by the solution conditions (esp. conductivity), cell membrane characteristics, and pattern of the applied field. Given a threshold of  $U_{\text{trans}} = 0.5 \text{ V}$ ,  $E$  must be maintained below 33 kV/m for a 20  $\mu\text{m}$ -diameter cell (or 66 kV/m for a 10  $\mu\text{m}$ -diameter cell).

**Table 3.1** Effect of Electric Field Gradient Length on  $F_{\text{DEP max}}$  for a 30 kV/m–0 kV/m Gradient

gradient length ( $\mu\text{m}$ )	$F_{\text{DEP max}}$ (pN)	
	$d = 10 \mu\text{m}$	$d = 20 \mu\text{m}$
300	1.7	13.3
200	2.6	19.9
100	4.9	39.9
50	10.2	80.1

## 3.4 MATERIALS AND METHODS

### 3.4.1 *Chemicals*

The RPMI 1640 media employed for cell culture was purchased from American Type Culture Collection (ATCC) (Manassas, VA). Ethylene glycol-propylene glycol block copolymer (Pluronic F108), bovine serum albumin (BSA) ( $\geq 98\%$  purity), and 1.0 M Tris·HCl stock solution were obtained from Sigma-Aldrich, Inc. (St. Louis, MO). The silicone elastomer and curing agent (Sylgard 184) used to prepare the poly(dimethylsiloxane) (PDMS) microfluidic devices were obtained from K. R. Anderson, Inc. (Morgan Hill, CA). All other chemicals were reagent grade and purchased from Fisher Scientific (Thermo Fisher Scientific, Inc., Waltham, MA) including sodium phosphate (mono- and dibasic), sucrose, and dextrose (d-glucose). All dilutions were carried out with Milli-Q water ( $18.0 \text{ M}\Omega \cdot \text{cm}$ ). DEP buffers were comprised of 8.0% sucrose, 0.3% dextrose, and 0.1% BSA in either 10 mM Tris (pH 8.1) or 10 mM phosphate (pH 7.2) buffer.

### 3.4.2 *Cell Culture*

Mouse pro-B BaF3 B-cells were obtained from ATCC. These B-cells were cultured in RPMI 1640 supplemented with 1% pen-strep and 10% fetal bovine serum at  $37^\circ \text{C}$  and 5%  $\text{CO}_2$ . The cells were subcultured every 3–4 days such that the concentration of cells did not exceed  $1 \times 10^6$  cells/mL. In preparation for DEP experiments,  $\sim 1 \times 10^6$  cells were pelleted by centrifugation followed by resuspension in 5 mL of the desired DEP buffer. This process was repeated one additional time to ensure cell culture medium components were removed.

### 3.4.3 *Device Fabrication*

PDMS/glass hybrid microfluidic devices with embedded Au BPEs were fabricated using standard photolithographic techniques.<sup>62</sup> Briefly, 1-mm-thick glass slides coated with 100 nm Au (no binding layer) were photolithographically patterned using SPR220-7.0 photoresist followed by wet-etching the Au in a 10% KI and 2.5% I<sub>2</sub> solution. The remaining photoresist was then dissolved with acetone. PDMS microchannels were molded by pouring precursor onto an SU-8 master and curing at 70 °C for 2 h. Reservoirs with 4-mm diameters were punched at both ends of each microchannel. The PDMS and Au-on-glass substrates were aligned and irreversibly sealed by the following process. First, both substrates were exposed to an O<sub>2</sub> plasma (plasma cleaner, Harrick Scientific, Ithaca, NY) for 1 min. Second, a drop of ethanol was applied to the glass substrate. Third, the PDMS monolith was put in contact with the glass substrate and aligned under a microscope. Then, the device was baked at 70 °C for 1 h to drive off ethanol. Finally, the device was filled with 3 μM Pluronic in either 10 mM Tris (pH 8.0) or 10 mM phosphate (pH 7.2) buffer selected to match the type of DEP buffer to be employed. The device was covered with parafilm and incubated at 4 °C overnight (at least 18 h). Pluronic coating served to dampen electroosmotic flow.<sup>63</sup>

The device dimensions were as follows. Dual parallel microchannels were each 4.0 mm long × 20 μm tall × 60 μm wide and separated by 400 μm. The channel inlets were tapered with a 53° angle leading to 4.0-mm-diameter reservoirs. The ceiling of the inlets was supported with diamond-shaped pillars (100 μm × 40 μm). This inlet geometry was designed to facilitate unimpeded introduction of cells into the microchannels. At the center of one microchannel (the DEP channel, Figure 3.2c), there was a 30 μm × 30 μm side chamber, which was aligned to the BPE tip. The exposed BPE tip was approximately 30 μm wide × 30 μm long (defined by

chamber). The auxiliary end of the BPE extended across the auxiliary channel (Figure 3.2c) and was 15  $\mu\text{m}$  wide.

#### 3.4.4 *DEP Experiments*

The combined AC/DC electric field was applied to four Pt wires dipped in the device reservoirs ( $V_1$ ,  $V_2$ ,  $V_3$ ,  $V_4$ , Figure 3.2c) using a Hewlett-Packard 33120A waveform generator (Hewlett-Packard, Palo Alto, CA) and Kepco Model BOP 1000 M amplifier (Kepco, Inc., Flushing, NY). The AC field frequency was maintained at 1.8 kHz, at which the Clausius–Mossotti factor is  $-0.5$  (maximum nDEP force) for B-cells under the conditions employed here. Prior to a DEP experiment, each microfluidic channel was rinsed with the appropriate DEP buffer (as indicated in the Results and Discussion section) for 1 min at 3 psi. The reservoirs were then filled with DEP buffer containing  $2 \times 10^5$  B-cells/mL. Where indicated in the Results and Discussion section, cell viability was tested by exposing DEP-trapped cells to 0.4% Trypan blue dye in DEP buffer for  $>5$  min.

### 3.5 RESULTS AND DISCUSSION

In this section, we describe nDEP attraction and repulsion of cells from a BPE and the impact of FIE and FID on these forces. We demonstrate nDEP repulsion of B-cells from a BPE in the absence of faradaic reactions (i.e., no DC field component). We then show that FIE at either the BPE anode or cathode leads to nDEP attraction that increases with increased AC field strength. These results are contrasted with nDEP repulsion of B-cells from an FID zone.

### 3.5.1 *nDEP at a BPE in the Absence of Faradaic Reactions*

Figure 3.3a demonstrates that a B-cell undergoes nDEP repulsion from a BPE tip in an AC-only electric field. In this experiment, the DEP channel (Figure 3.2c) was rinsed with DEP buffer (8.0% sucrose, 0.3% dextrose, and 0.1% BSA in 10 mM Tris (pH 8.0)), and then, it was filled with the same DEP buffer containing  $2 \times 10^6$  B-cells/mL. The auxiliary channel was rinsed and filled with 10 mM NaCl as an electrolyte.

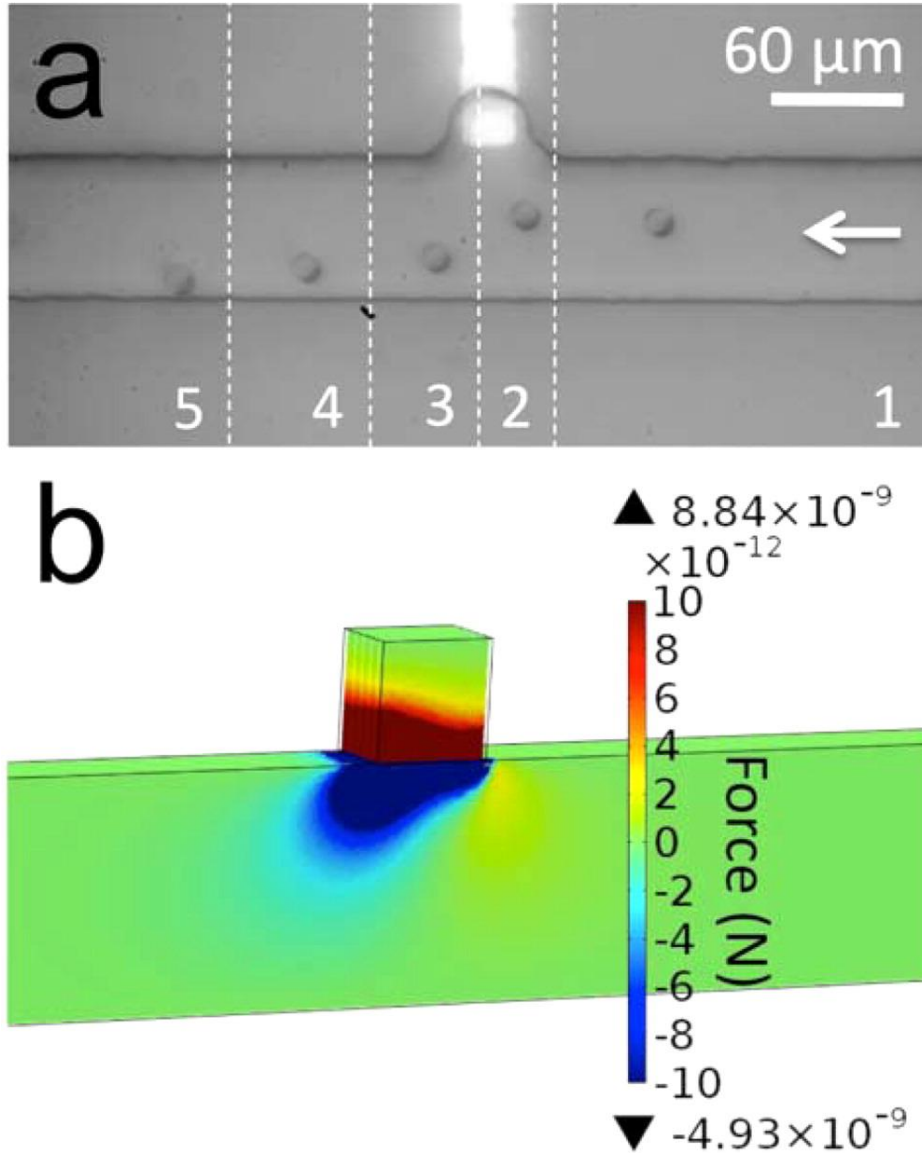


**Figure 3.3.** (a) A series of optical micrographs, which show nDEP repulsion of a B-cell from the BPE tip under AC-only electric field in Tris DEP buffer. Each image slice (numbered sequentially 1–5) is separated by 2.5 s.  $E_{\text{RMS,avg}} = 5.7 \text{ kV/m}$  ( $t = 0 \text{ s}$ ) to  $17.7 \text{ kV/m}$  ( $t = 5 \text{ s}$ ). (b) Simulated magnitude of the  $y$ -component of  $F_{\text{DEP}}$  in the  $xy$ -plane at  $z = 5 \mu\text{m}$ .

Flow (right to left, Figure 3.3a) was established in the DEP channel by introducing a solution height differential in the reservoirs at its ends such that the average linear flow velocity  $v_{\text{avg}} = 20 \mu\text{m/s}$ . An AC voltage of 64 Vpp at 1.8 kHz was applied to the left-hand reservoir of the DEP channel (V<sub>3</sub>, 3.2c), and the remaining three reservoirs were grounded. Under these conditions, the spatially averaged root-mean-square (RMS) electric field strength along the DEP channel was  $E_{\text{RMS,avg}} = 5.7 \text{ kV/m}$ . As the cell approached the BPE,  $E_{\text{RMS,avg}}$  was increased stepwise (from 1 V peak-to-peak (Vpp) to 6 Vpp on the waveform generator at 1 Vpp per second) from 5.7 kV/m at  $t = 0 \text{ s}$  (slice 1) to 17.7 kV/m at  $t = 5 \text{ s}$  (slice 3). The cell was briefly attracted toward the BPE and then repelled by nDEP from the locally high electric field around the BPE tip. The greatest deflection (between slices 2 and 3) is 20  $\mu\text{m}$  over 2.5 s, which requires  $\sim 1 \text{ pN}$  of force. This result is significant because it establishes (1) that these AC field strengths are sufficient to exert nDEP force and (2) the electric field strength around the BPE is a local maximum in the absence of faradaic current and FIE. These results are corroborated by numerical simulations of  $F_{\text{DEP}}$ , in which  $i_{\text{BPE}} = 0$  and  $E_{\text{RMS,avg}} = 25 \text{ kV/m}$ . Figure 3.3b shows the simulated y-component of  $F_{\text{DEP}}$  ( $F_{\text{DEP,y}}$ ) surrounding the BPE in the  $xy$ -plane located at  $z = 5 \mu\text{m}$  above the BPE and channel floor. Negative values of  $F_{\text{DEP,y}}$  indicate nDEP repulsion (in the negative direction on the y-axis). The magnitude of  $F_{\text{DEP,y}}$  ranges from  $-320 \text{ pN}$  to  $760 \text{ pN}$ . However, several cell diameters from the BPE,  $F_{\text{DEP,y}}$  is nearer to  $10 \text{ pN}$ , which is consistent with typical  $F_{\text{DEP}}$  magnitudes  $10\text{--}20 \mu\text{m}$  from an electrode surface.<sup>64,65</sup> At the channel midline,  $F_{\text{DEP}}$  has decreased to  $< 2 \text{ pN}$ . Details of the simulation are included in the Supporting Information (SI). Most importantly, the simulation correctly predicts the trajectory of the B-cell as it traverses

the channel from right to left. There is weak (several pN) attraction of the cell (positive  $y$ -direction) to the right of the BPE followed by further-reaching repulsive forces.

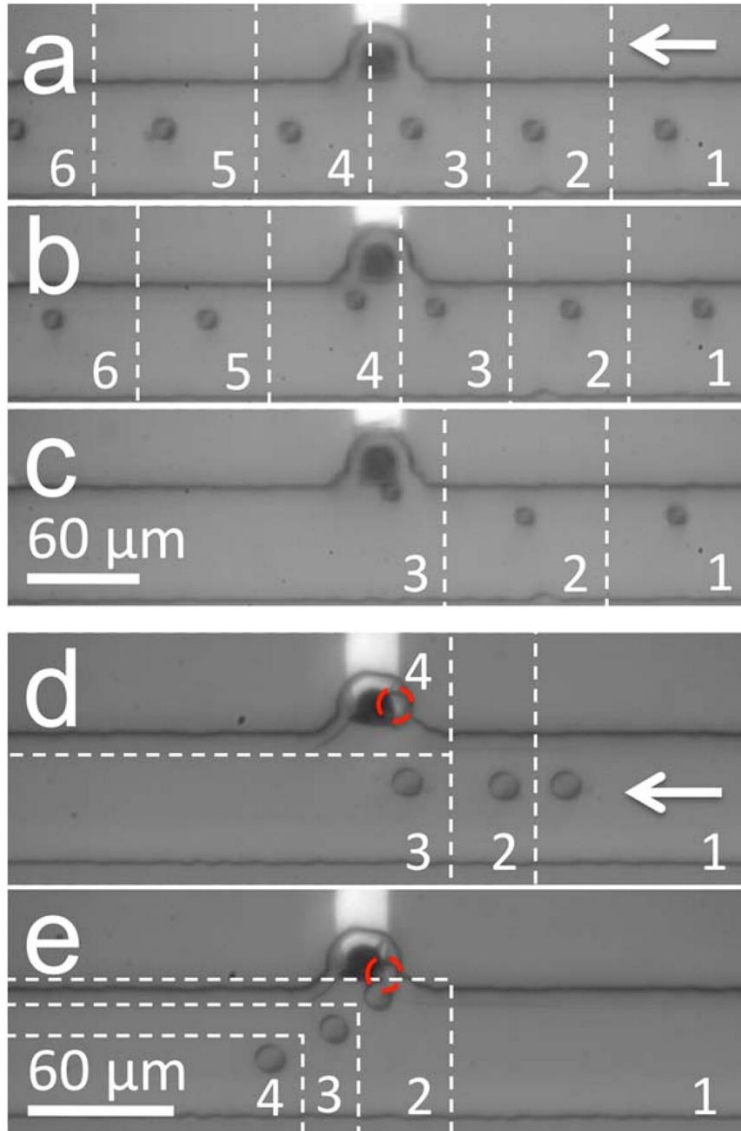


**Figure 3.4.** (a–c) Multiple series of optical micrographs showing increasing nDEP attraction of a B-cell toward the BPE anode in Tris DEP buffer.  $E_{DC,avg} = 0.75$  kV/m,  $E_{RMS,avg}$  for (a) 5.7 kV/m, (b) 13.3 kV/m, (c) 17.7 kV/m. Image slices are 1 s apart. (d) nDEP attraction of a B-cell toward the BPE cathode in phosphate DEP buffer (4 s/slice).  $E_{DC,avg} = 1.5$  kV/m,  $E_{RMS,avg}$  increased from 5.7 kV/m to 28.3 kV/m from  $t = 0$  s (slice 1) to  $t = 8$  s (slice 3). (e) Release of the trapped cell (2 s/slice) from (d) upon subsequent decrease of  $E_{RMS,avg}$  to 5.7 kV/m (from slice 1 to slice 2).

### 3.5.2 nDEP Attraction of a B-Cell to an FIE Zone at the BPE Anode and the BPE Cathode

In the previous subsection, we established that an AC field alone results in nDEP repulsion of B-cells from the BPE tip. Here, we demonstrate nDEP attraction to the BPE with the addition of a DC offset. The DC field can drive faradaic current ( $i_{\text{BPE}}$ ) leading to an FIE zone at either a BPE anode or a BPE cathode. Due to the negative charge of the cell membrane, in these two cases DEP force works with and against electrophoretic (EP) force, respectively. First, we will examine nDEP attraction of a B-cell to an FIE zone at the *BPE anode* in Tris DEP buffer (Figure 3.4a–c). In this device, nDEP cell trapping proceeded at the BPE anode as follows. First, the channels were rinsed and filled as described in the previous subsection. Then, flow was established as before such that  $v_{\text{avg}} = 65 \mu\text{m/s}$ . An AC field with a *negative* DC offset was applied at  $V_3$  versus ground ( $V_1$ ,  $V_2$ , and  $V_4$ ) such that  $E_{\text{RMS,avg}} = 5.7 \text{ kV/m}$  AC and  $E_{\text{DC,avg}} = 0.75 \text{ kV/m}$  DC. Figure 3.4a shows the resulting cell trajectory in 1 s slices. Under these conditions, the EP force exerted by the BPE anode was insufficient to attract and trap the B-cells. However, as the AC field strength was increased (Figure 3.4a–c;  $E_{\text{RMS,avg}} = 5.7, 13.3, \text{ and } 17.7 \text{ kV/m}$ , respectively) cells were increasingly attracted and finally trapped. This finding is significant because nDEP attraction toward the BPE indicates that the electric field is depressed around the BPE by FIE. At later time points than those displayed in Figure 3.4c, the trapped cell was pulled into the microchamber and remained over the BPE.

This result is attributed to an averaged axial electric field profile like that shown in Figure 3.2b (dashed line indicating “FIE”) caused by the progression of the oxidation reaction described by eq 1 leading to the accumulation of ionic species around the BPE. This ion enrichment zone decreases  $E$  locally. Importantly, although  $E$  is zero above the BPE whenever  $i_{\text{BPE}}$  is nonzero (solid and dashed lines, Figure 3.2b), cells can only be attracted to this region after an FIE zone

forms. In a control experiment, many cells were trapped under similar trapping conditions but on a larger area BPE, which extended across the DEP channel. These cells were tested for viability by flowing 0.4% Trypan blue in DEP buffer for >5 min. The cells did not uptake Trypan blue, thus indicating intact membrane integrity and viability. However, cells exposed to more positive or negative DC voltages after trapping but before exposure to Trypan dye were stained blue, indicating membrane degradation.

Likewise, we carried out nDEP trapping of a B-cell at the BPE *cathode* (Figure 3.4e–d). In this case, a similar device was filled with 10 mM phosphate (pH 7.2) in 8% sucrose, 0.3% dextrose, and 0.1% BSA (phosphate DEP buffer). An AC field with a *positive* DC offset was applied at  $V_3$  such that  $E_{\text{RMS,avg}} = 5.7$  kV/m AC and  $E_{\text{DC,avg}} = 1.5$  kV/m DC. Water reduction followed by deprotonation of phosphate species led to ion enrichment around the BPE tip. As the AC field strength was increased gradually from 5.7 kV/m to 28.3 kV/m, the cell was pulled into the chamber by nDEP (Figure 3.4d, 4 s/slice), and as the AC field was returned to 5.7 kV/m, the cell was expelled from the chamber (Figure 3.4e, 2 s/slice). This result is significant for two reasons. First, as in the previous experiment, this result demonstrates that faradaic current leading to FIE sufficiently decreases the local electric field around the BPE to reverse the role of nDEP from repulsion to attraction. Second, in this case, the cell was trapped by nDEP force despite electrostatic repulsion of the negatively charged cell from the BPE cathode. The role of EP is underscored by the immediate expulsion of the cell from the chamber once the AC field strength was decreased (Figure 3.4e). In both of these cases,  $F_{\text{DEP}}$  ranges from 1 to 3 pN, which is similar in magnitude to the control of Figure 3.3a (no FIE) but with a reversed sign. Here, the force is weak because the electric field gradient is formed based on a decrease in local field strength, and both the magnitude and slope of the field contribute to  $F_{\text{DEP}}$ .

This result has been repeated with the BPE misaligned from the chamber such that the two features are laterally separated by 50  $\mu\text{m}$  and the BPE extends 15  $\mu\text{m}$  into the channel (results not shown). In this control experiment, regardless of the direction of flow, cells favored trapping at the BPE rather than the chamber. This result verifies that the zero electric field directly above the BPE and FIE depression of the surrounding field are the primary mechanisms responsible for cell trapping.

Furthermore, we performed a control with no BPE (results not shown). While the electric field in an empty chamber (no BPE) is lower than that in the microchannel, at AC field strengths up to  $E_{\text{avg}} = 28.3 \text{ kV/m}$ , cells are only weakly attracted to the chamber and are only drawn into it under stopped-flow conditions.

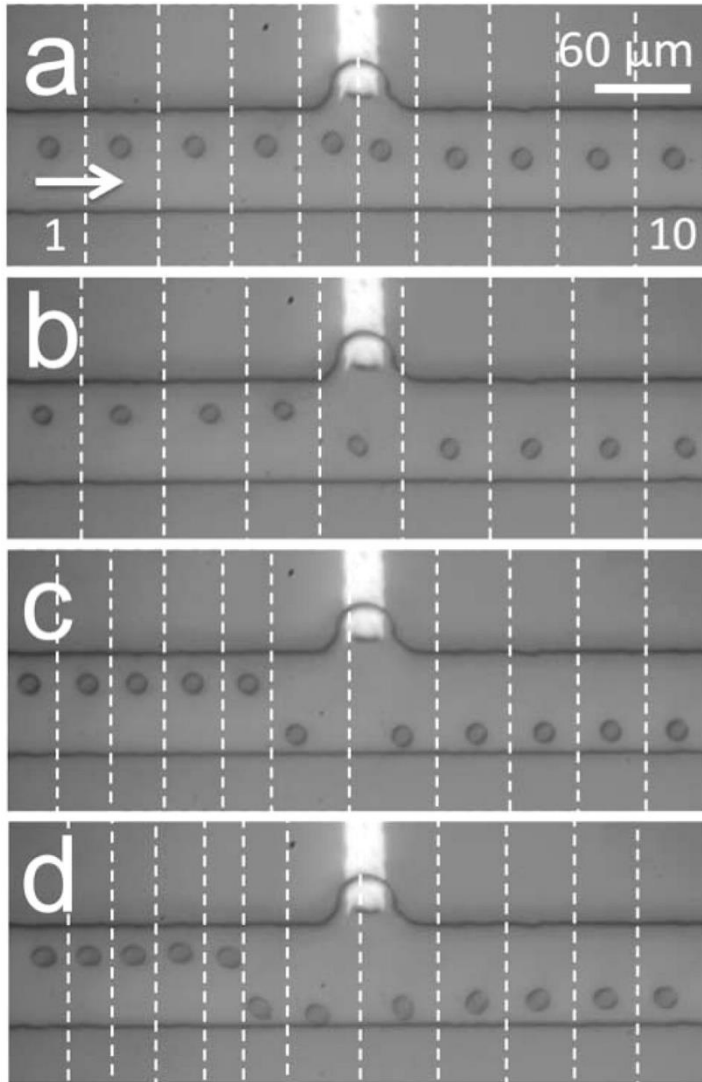


**Figure 3.5.** (a–d) Multiple series of optical micrographs, which demonstrate nDEP repulsion of individual B-cells from an FID zone at the BPE cathode in Tris DEP buffer (0.5 s/slice).  $E_{DC,avg} = 1.25$  kV/m.  $E_{RMS,avg}$  is (a) 0.57 kV/m, (b) 6.13 kV/m, (c) 7.95 kV/m, and (d) 10.25 kV/m.

### 3.5.3 *nDEP Repulsion of a B-Cell from an FID Zone*

Just as crucial as an understanding of the impact of FIE on  $F_{\text{DEP}}$  is an examination of the FID regime. The enhanced local electric field strength associated with ion depletion can lead to enhanced EP exclusion of particles, thus, complicating the delineation of DEP and EP forces in the FID zone. To separately interrogate the role of nDEP in cell repulsion from an FID zone, we once again increased the AC field contribution while maintaining a constant DC component. In this experiment, the device was prepared with 10 mM Tris DEP buffer (DEP channel) and 10 mM NaCl (auxiliary channel) as described in previous subsections. A flow rate of  $v_{\text{avg}} = 85 \mu\text{m/s}$  (left to right) was established in the channel. An AC field with a *positive* DC offset was applied at  $V_3$  such that  $E_{\text{RMS,avg}} = 0.57 \text{ kV/m}$  and  $E_{\text{DC,avg}} = 1.25 \text{ kV/m}$  DC. Water reduction at the BPE cathode followed by neutralization of  $\text{TrisH}^+$  ions (eqs 3 and 4) led to ion depletion around the BPE tip. Figure 3.5a–d (0.5 s/slice) show increasing degrees of nDEP repulsion of a B-cell from the resulting FID zone as the AC field strength was increased from  $E_{\text{RMS,avg}} = 0.57 \text{ kV/m}$  to 6.13, 7.95, and then 10.25 kV/m, respectively. The DEP force exerted on the  $\sim 12\text{-}\mu\text{m}$ -diameter cells at the greatest measured deflection (between 0.5-s slices) was estimated as 1.2, 4.7, 6.6, and 7.6 pN, respectively. The force gained an  $\sim 0.7 \text{ pN}$  per 1 kV/m increase in  $E_{\text{RMS,avg}}$  over this range. The key point is that by simply changing the identity of the DEP buffer from phosphate, which creates an FIE zone in the presence of  $\text{OH}^-$ , to Tris, which is neutralized under the same conditions, cells go from being pulled into the chamber (Figure 3.4d) to colliding with the opposing channel wall (Figure 3.5d). Furthermore, we have demonstrated that the causative force is dielectrophoretic. nDEP repulsion of cells from an FID zone formed at the BPE *anode* in phosphate DEP buffer was also performed.

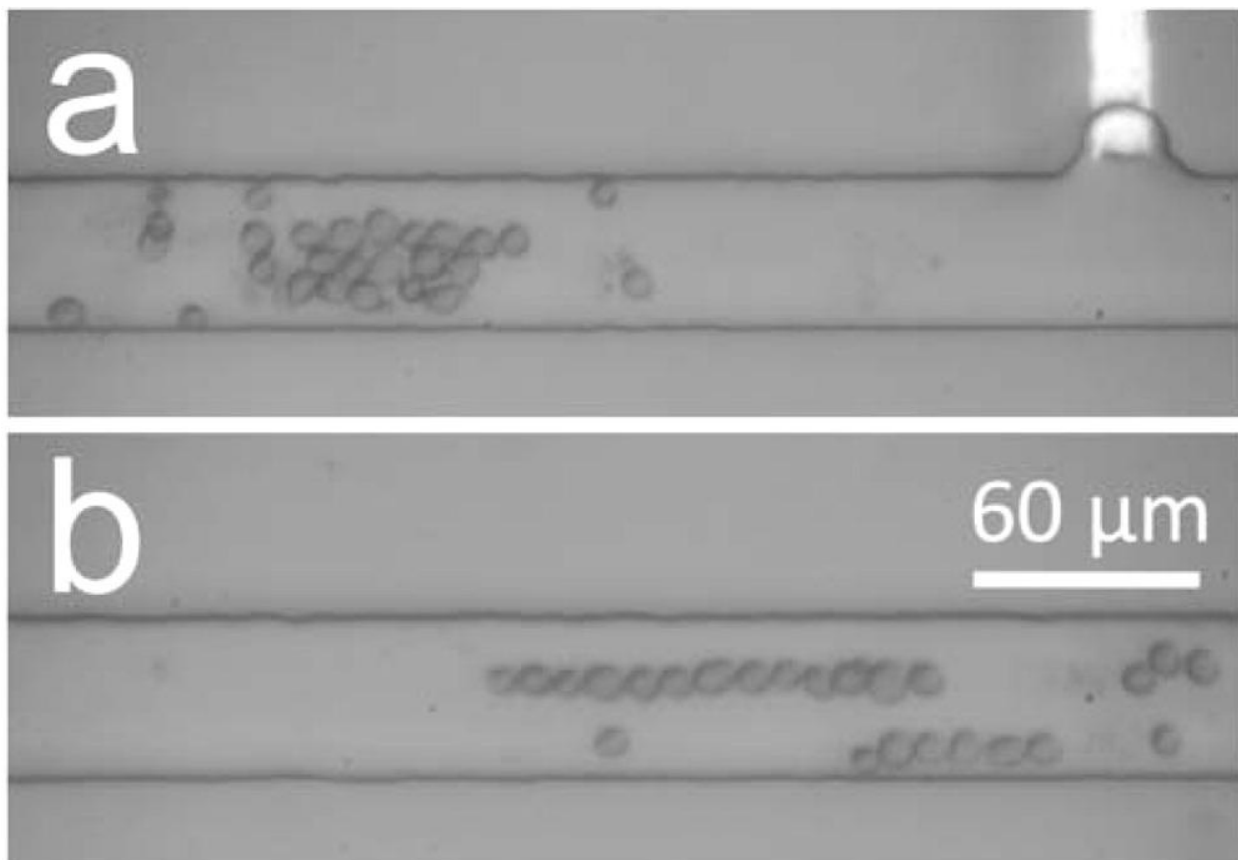


**Figure 3.6.** Sequential optical micrographs showing nDEP and EP repulsion of B-cells from an FID zone at the BPE cathode in Tris DEP buffer ( $E_{DC,avg} = 2.5$  kV/m) with  $E_{RMS,avg}$  of (a) 0.57 kV/m and (b) 10.25 kV/m.

In the experiment described in the above paragraph, the flow rate and faradaic reaction rate were selected such that cells could circumvent the FID zone. Figure 3.6a and 3.6b show cells repelled by a stronger and larger FID zone ( $E_{DC,avg} = 2.5$  kV/m) at the same flow rate (85  $\mu\text{m/s}$  left to right) as was employed in Figure 3.5a–d. It is important to note that EP repulsion of the negatively charged cells by the enhanced local electric field around the BPE cathode likely plays a significant role at this DC field strength. At low AC field strength ( $E_{RMS,avg} = 0.57$  kV/m, Figure 3.6a), cells were impeded and accumulated along the electric field gradient formed by the FID zone where the force of electrophoresis and opposing fluid flow on the cells balanced (approximately 9.5 pN). We have also observed this effect with a DC-only field. When the AC field was subsequently increased to  $E_{RMS,avg} = 10.25$  kV/m, the additional nDEP force transported the cells to a new balance point  $>450$   $\mu\text{m}$  from the BPE (Figure 3.6b, image shifted 450  $\mu\text{m}$  to the left versus Figure 3.6a). Pearl chaining was observed under these conditions due to the high AC field strength and fixed location of the cells. Importantly, the FID zone extends the reach of DEP force to several hundred microns from the BPE. Given a larger channel width, we anticipate that cells would be able to circumvent the large FID zone, albeit at several hundred microns from the BPE. These results also demonstrate the many roles of the DC field component: activation of the BPE ( $i_{BPE} \neq 0$ ), control of FIE/FID zone size, and EP force. Therefore, the strength of the DC field is critical to DEP outcomes in a BPE-based device.

### 3.6 CONCLUSION

In conclusion, we have demonstrated both nDEP attraction and repulsion of biological cells from each a BPE cathode and anode including single cell sequestration in a side chamber. Furthermore, we have shown that the direction, magnitude, and extent of nDEP force can be controlled via faradaic reactions at the BPE, which impact the local conductivity of the DEP medium through the formation of FIE and FID zones. Numerical simulations quantifying the contribution of FIE and FID are in progress.

As a natural extension of this work, we are investigating several BPE array formats for array-based single-cell trapping and isolation. This technology will provide a powerful tool for parallel single-cell analysis. Additionally, we aim to exploit the selectivity of DEP for individual cell types. We anticipate that, at an AC frequency that produces distinct values of  $F_{\text{DEP}}$ , repulsion of cells from an extended FID zone will yield high-throughput sorting. Finally, these principles will extend to the pDEP regime (higher AC field frequencies) at which higher DEP forces will result due to a maximum value of the real part of the Clausius–Mossotti factor ( $\text{Re}[K(\omega)] = 1$ ).

Chapter 4.

ISOLATION OF CIRCULATING TUMOR CELLS  
FROM WHOLE BLOOD WITH HIGH PURITY  
USING A SEQUENTIAL SORTING SCHEME

## 4.1 ABSTRACT

Cancer metastasis is an important research area for the improvement of cancer outcomes. Of great importance to understanding metastasis is the isolation of cancer cells from the blood of patients with potential metastatic disease. These cells, called circulating tumor cells (CTCs), are shed from the primary tumor and are present in the blood in low numbers, and can be isolated based on their physical and molecular differences from other cells in circulation. While counting CTCs can be a useful tool in predicting cancer prognosis, more in-depth study of CTCs facilitated by downstream analysis can yield understanding of metastasis that can lead to better treatments, the ultimate goal of all cancer research. CTCs are difficult to detect, due to their low abundance and heterogeneity. Previously, we have reported a CTC isolation platform with high throughput, high sensitivity and clinical validation, ensemble decision aliquot ranking (eDAR). This platform can achieve greater than 90% recovery for cultured cancer cell lines and is also capable of detecting cells in clinical samples, including cells with low expression of traditional CTC markers, which have been linked to greater metastasis. These cells are of great interest for furthering our understanding of the metastatic cascade and developing new treatments. Here, we demonstrate an improved eDAR device capable of isolating CTCs from whole blood with greater purity (70% vs 1%) and depositing the cells into a 96-well plate for further study. This is achieved *via* a sequential sorting design, where whole blood is sorted, the aliquot stretched, and then sorted again to improve purity. With the improved purity of this device, it now is possible to collect the cells in a 96-well plate, and this design is amenable to coupling with a dispensing system to achieve one-cell-per-well results, averaging less than one contaminating white blood cells per CTC.

## 4.2 INTRODUCTION

Here we report the isolation of circulating tumor cells (CTCs) from whole blood using a microfluidic sequential sorting scheme. This is a key improvement on our microfluidic CTC detection platform, ensemble decision aliquot ranking (eDAR), for two reasons. First, by sorting the aliquot a second time, the cell of interest can be further separated from other blood cells and thus the purity improved. Passive mixing features to stretch the sorted aliquot are employed between the two sorts to further improve the separation and purity. Second, the cells can be collected in a 96-well plate, making them accessible to further analysis. In previous work, the cells were collected in an on-chip filter, where they could be labeled and counted, but not easily removed. With this new platform, cells are flowed out of the chip upon being sorted a second time, and are collected in a 96-well plate. This enables the possibility of integrating eDAR with an automated dispensing system.

The rare-cell isolation platform developed in our lab consists of an optical detection system, a microfluidic sorting scheme and an on-chip filter for enumeration. The optical detection system uses laser-induced fluorescence (LIF) detection across the width of a microfluidic channel. Cells in labeled whole blood samples can be detected in multiple colors, and can be simply enumerated from the detection trace<sup>7</sup>. To improve the system, we developed a sorting scheme, which consists of a junction as shown in Figure 1.2, where upon detection, sorting can be diverted to another channel leading to an on-chip filter. Cells collected can be fixed, permeabilized and labeled with additional antibodies prior to enumeration. Some recent advances to this platform include a dual-capture scheme<sup>32</sup>, where cells labeled with different antibodies can be sent to two different filters, a sequential bleaching and relabeling scheme<sup>66</sup>, a calibration of the system for the limit of detection (LOD) in terms of surface antigens<sup>67</sup>, and a

demonstration of improved detection of circulating tumor cells expressing low levels of the commonly used surface marker, EpCAM, using a cocktail labeling scheme<sup>67</sup>.

CTCs remain an analytical challenge to detect and isolate, owing to their low abundance in whole blood (10s to 100s per ml whole blood)<sup>2,10,11</sup> and their heterogeneity<sup>3</sup>. However, due to their importance in metastasis, overcoming these challenges remains an important area of scientific research. A variety of approaches have been taken to isolate CTCs, with most falling into two categories: antibody-based methods and physical methods. Physical methods include isolation based on size or electrochemical characteristics. CTCs are, on average, larger than blood cells, and thus can be isolated by filtration<sup>22–26,68</sup> or flow fractionation<sup>69</sup>. While filtration is a fast and simple method, the overlap in size between CTCs and white blood cells<sup>27</sup> means that purity will always be low and the increased deformability of CTCs compared to other epithelial cells means that they can be difficult to remove from the filter for further analysis. Recently, platforms have been developed that use the differential flow patterns of CTCs in microfluidic channels to isolate them from other blood cells<sup>70</sup>. While these methods leave the cells more accessible than filtration based methods, they suffer from low purity as well and can be complicated to implement. One method to overcome the lower purities is to pass the collected cells through the device a second time<sup>69</sup>. Dielectrophoretic methods instead detect cells based on their different electrochemical properties, which will include size, but has the potential to be more sensitive due to membrane and structural differences between CTCs and white blood cells<sup>71</sup>. While physical methods of isolation are promising because they do not require labeling steps, they are limited due to the overlap between the size distributions of white blood cells and CTCs; to detect the smallest CTCs, purity must be sacrificed.

Three main ways of utilizing antibodies can be found in the literature: magnetophoretic detection, where blood is labeled with antibodies bound to magnetic beads and magnetic fields are employed to separate CTCs<sup>15,16</sup>; surface capture, where antibodies are bound to posts or other features of a microfluidic chip and CTCs are captured on-chip<sup>18-21</sup>; and fluorescent based methods, where blood is labeled with fluorescently-bound antibodies and CTC's detected with LIF. While the only FDA approved platform, CellSearch, employs magnetic detection<sup>72</sup>, it is unclear if this method can be sensitive enough to detect CTCs expressing low levels of surface antigen. Surface capture methods have been widely published, and remove the necessity of labeling blood with antibodies by instead having the antibodies bound to the chip for capturing cells. However, sensitivity can be low and is dependent on CTCs making sufficient contact with posts or channels. While this is limited in microfluidic systems by the nature of laminar flow, some recent advances use herringbone structures to increase mixing and improve this method<sup>73</sup>. Herringbones were developed by Whitesides and co-workers in 2002 to improve mixing in microchannels<sup>74</sup>. All the antibody-based methods have the potential to isolate cells with high purity, due to the specificity of epithelial antibodies such as EpCAM for CTCs. However, fluorescent based methods provide a promising way to detect, enumerate and isolate CTCs, as these methods have been shown to detect cells down to a LOD of 23,000 surface antigens<sup>67</sup>, whereas most other methods only report recovery rates of high expressing cell lines like MCF7.

A combination of high sensitivity, high recovery and high purity are essential for a successful CTC isolation method. Additionally, collecting the cells in a way that they are available for downstream analysis is becoming increasingly important as CTC heterogeneity becomes clearer. Our platform, eDAR, has been previously demonstrated to be highly sensitive, detecting cells with low epithelial expression that have undergone the epithelial-to-mesenchymal

transition and may be more metastatic. Here, we present a sequential eDAR chip, where a blood aliquot is sorted, stretched, and sorted again to increase purity. Simply sorting a second time increases the purity from 1% to 17%. Stretching features, including increased channel length and herringbones to chaotically mix the sample, can further improve this up to 70%. Since the second sorting happens on the same microfluidic chip, minimal additional time is needed and 1 ml of blood can be run in 30 min. Additionally, cells are now collected in a 96-well plate, enabling downstream analysis of sorted CTCs.

## 4.3 MATERIALS AND METHODS

### 4.3.1 *Cell culture.*

MCF-7 cell line was obtained from American Type Culture Collection (ATCC, Manassas, VA). Cells were cultured at 37 °C and 5% CO<sub>2</sub> in EMEM media (ATCC). Media was supplemented with 5% v/v fetal bovine serum (FBS) and 1% v/v penicillin streptomycin (both from Sigma, St Louis, MO).

### 4.3.2 *Blood samples.*

Healthy, whole blood samples were obtained from PlasmaLab International (Everett, WA).

### 4.3.3 *Reagents.*

Antibodies were purchased from BioLegend, Inc. (San Diego, CA) apart from phycoerythrin (PE)-anti-EpCAM (Abcam, Cambridge, MA). Isoton II buffer, used as a sheath flow for eDAR, was purchased from Beckman Coulter (Brea, CA). Bovine serum albumin (BSA) and TWEEN 20 were purchased from Sigma (St. Louis, MO). Two solutions were

prepared in isoton: one at 0.1% BSA w/w used for labeling and the second at 1% BSA/0.05% TWEEN20 w/w and used for pretreating materials. Glycerol was purchased from EMD (Billerica, MA) and a 25% w/w solution was prepared in Isoton to simulate the fluidic characteristics of blood for sorting experiments. This solution was mixed in a 30/70 ratio with green food dye (COV Extract Company, Rockford OH) for experiments where images of the sorting were needed.

#### 4.3.4 *Microfluidic chips.*

Silicon masters were made as described previously<sup>10</sup>. Briefly, silicon masters were made using standard photolithographic techniques using SU-8 2050 (MicroChem, Westborough, MA) for spin coating. Chips were made from PDMS in a 1:10 ratio of precursor to polymer base, fully cured, and sealed to a glass substrate immediately following exposure to O<sub>2</sub> plasma for one minute. If not used immediately, chips were covered and stored until use, but not longer than one month.

#### 4.3.5 *Testing of sequential sorting chip designs for dye stretching.*

To test different chip designs for their ability to stretch an aliquot, 10  $\mu$ l PE-goat-anti-mouse antibody was added to 40  $\mu$ l filtered isoton in a centrifugal filter tube (EMD Millipore, Billerica, MA) and spun at 14,000 RPM for 5 min to remove aggregates. This was added to 1 ml 25% glycerol solution w/w in isoton. Approximately 10 $\mu$ m 1500 yellow fluorescent beads (Duke Scientific, Palo Alto, CA) were added. The sample was run on a sequential eDAR chip and sorting established. The APD trace was collected, using the beads to trigger sorting events, and sorted dye peaks were analyzed.

#### 4.3.6 *Purity tests with sequential eDAR.*

MCF7 cells were labeled with 30  $\mu$ l PE-anti-EpCAM for 3 hours. After washing, cells were counted and approximately 100 cells were spiked into 0.5 ml blood. Blood was sorted on a sequential eDAR chip. Upon establishing sorting, a fresh tube, pre-treated with 1% BSA 0.05% TWEEN20, was plugged into the collection outlet and run into a pre-treated 15ml centrifuge tube. After sorting, collected cells were spun down at 450 RCF for 10 min, and supernatant removed. 15  $\mu$ l PE-anti-CD45 (spun to remove aggregates) was added for 3 hours. The sample was washed with isoton + 0.1% BSA and run on a new eDAR chip, only punched in the inlet and outlet for ease of use. The trace was collected and total PE labeled cells counted using MATLAB analysis. As a control, the above process was repeated without the addition of PE-anti-CD45 and the PE peaks were counted and confirmed to match with the number of PE peaks from the first sorting experiment.

#### 4.3.7 *Sequential eDAR recoveries.*

MCF7 cells were labeled with 30  $\mu$ l PE-anti-EpCAM (spun to remove aggregates) for 3 hours. After washing, cells were counted and a known quantity (~100 cells) were spiked in to 0.5 ml blood. Blood was sorted on a sequential eDAR chip. Upon establishing sorting, a fresh tube, pre-treated with 1% BSA 0.05% TWEEN20 was plugged into the collection outlet and run into a pre-treated 96-well plate. Cells were collected into the wells of the 96-well plate, manually moving the tube into a new well when a volume of ~250  $\mu$ l was reached. Upon completion of sorting, the well plate was spun down at 450 rcf for 10 min. Cells were imaged and counted on a Nikon TE 2000 U microscope with a 20X, 0.75 NA objective (Nikon, Tokyo, Japan).

## 4.4 RESULTS AND DISCUSSION

### 4.4.1 *Two-stage sorting improves purity.*

Since eDAR sorts aliquots of whole blood instead of analyzing the cells single file, the running time for a sample is greatly reduced compared to other fluorescent sorting methods. However, inherent to this method is the fact that blood cells will be sorted with the labeled cell of interest. For previous iterations of eDAR, an on-chip filter was used to collect the cells, with slits 5  $\mu\text{m}$  wide. This allowed all the red blood cells and most of the white blood cells to pass through, while retaining even the smallest CTCs. However, cells retained on the filter were time consuming to remove, and the need for improved purity arose if cells were going to be collected directly after sorting. To achieve this, we designed a new chip to include a second sorting junction after the first (see Figure 4.1). The sorted plug is stretched as it passes down the channel separating the two junctions, and there is a second detection and sorting once the cell reaches the second junction. There are two detection spots, one just before each sorting junction as shown in Figure 4.1a. Figure 4.1c-d show the detection trace from the two junctions during a sort. Cells are detected in both junction, as seen on the plots. Figure 4.1e shows a shorter section of the combined trace of the APD data from the first sorting junction and the second sorting junction, shown in green and blue respectively. There is a delay time between the sorts, during which the aliquot is stretched and diluted. This means that the concentration of blood cells is reduced, and the number of these cells sorted a second time is much lower, thus improving the purity, as measured as number of CTCs sorted per sample divided by the total nucleated cells collected.

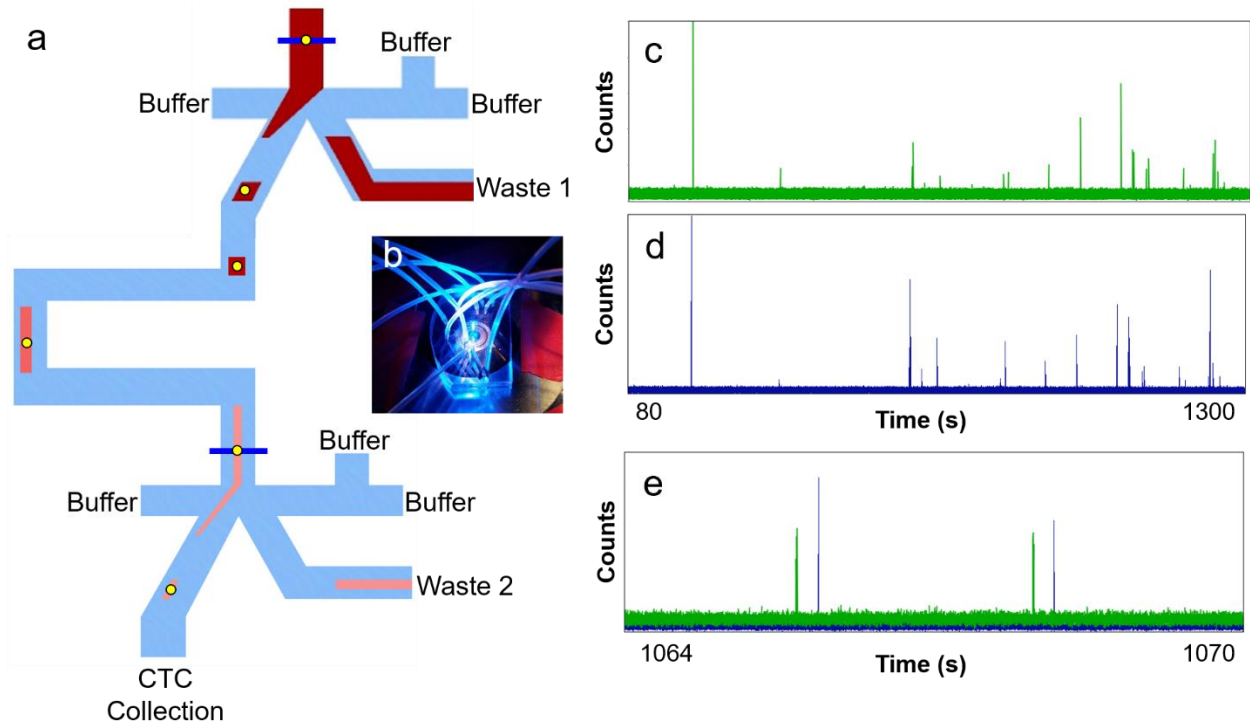


**Figure 4.1 a** Detail of the sequential eDAR chip. Blood is flowed onto the chip and detected at an LIF detection line. This triggers a sorting event by turning on a solenoid and increasing flow from the right side of the junction. The aliquot passes down a channel and encounters another LIF detection line, where it is sorted again. Since the aliquot is stretched between the junctions, fewer blood cells are sorted the second time and instead flow into waste 2. **b** Image of chip mounted on microscope when sample is running with 488 nm laser **c-d** APD trace of a sorting experiment. The first sorting junction is shown in blue (**c**) and the second in green (**d**), with time in seconds on the x-axis and counts (a measure of the electrical signal to the APD) on the y-axis. **e** A section from **c** and **d** combined to show the sorting event in the first channel, followed by the sorting event in the second channel.

To quantify this improvement, MCF7 cells were labeled with PE-anti-EpCAM, washed, counted, and spiked into 0.5 ml of healthy blood. Blood was flowed onto a sequential sorting chip at a rate of 30  $\mu\text{l}/\text{min}$  and sorting established by adjusting sheath flow pressures. Once stable sorting pressures were set, the collection outlet tubing was removed and pre-treated tubing (1% BSA and 0.05% tween20 in Isoton) inserted. The outlet from this tubing was placed in a pre-treated 15-ml centrifuge tube and the entire sorted volume, which contains the sorted MCF7

cells, blood cells sorted in each aliquot, and isoton buffer sheath flow, collected. For a sorting experiment with 0.5 ml of blood, this volume was approximately 1 ml. After sorting, the collected volume was centrifuged at 450 rcf for 10 min and supernatant carefully removed to ~300  $\mu$ l. 15  $\mu$ l of PE-anti-CD45 was added and cells were labeled for 3 hours, washed, and the supernatant removed down to 1 ml. This was run through a clean eDAR chip, only punched at the inlet and one outlet, and the APD trace collected and analyzed. As a control, the above process was conducted without the addition of the PE-anti-CD45 antibodies, and the number of PE peaks correlated with the number of PE peaks from the first sorting experiment, thus confirming that cells are not lost during the labeling process.

The number of peaks in the trace yields the total nucleated cells sorted, both the PE-labeled MCF7 cells from the initial sorting and the PE-labeled white blood cells labeled after sorting. To calculate the purity, the number of MCF7 cells sorted was divided by total nucleated cells. The number of MCF7 cells sorted was obtained from number of sorting events in the first sorting experiment. For 1-stage sorting, we calculated a purity of 1%. For a 2-stage sort, where the two junctions are separated by a 3-cm channel, we achieve a 17% purity.

#### 4.4.2 *Lengthening the channel between the two sorting junctions can improve the purity.*

The data presented above for a 3-cm straight channel separating the two junctions shows a 17X increase in purity. This is driven by the stretching and diluting of the aliquot as it travels between the two sorting junctions. Since mixing is low in laminar flow in microchannels, longer channels are needed to achieve substantial mixing. Thus, the easiest way to improve the purity would be to lengthen the channel between the two junctions. Two chip were designed and manufactured with a 5.5 cm channel and a 8.8 cm channel separating the two junctions, and

purities were measured as previously described. The 5.5 cm channel yielded a purity of 21%. The 8.8 cm channel yielded a purity of 32%.

#### 4.4.3 *Manipulating the channel between the two sorting junctions can improve the purity.*

While lengthening the channel between the junctions improves the stretching and the purity, the length of channel needed to drastically improve purity and approach single-cell isolation is unrealistic. Thus, a more aggressive mixing or separation strategy is needed. There are three ways we employed to stretch the aliquot and improve the purity. One, we designed a “flow stretcher”, which consisted of a long channel connected by a series of smaller channels (see figure 4.2B), such that part of the aliquot would go down the first small channel and part would continue down the main channel, until the aliquot had been completely separated into many smaller aliquots.

To test this, PE dye was flowed onto the chip in a glycerol solution containing fluorescent beads and sorting established. The sorted aliquot contained the yellow fluorescent bead and a plug of dye, and the improvement to the purity could be estimated from the stretching of the dye aliquot, as visualized by the APD trace, right before the second sorting junction. While this would not give the absolute purity, it was a useful method for comparing between device designs. The longer the aliquot was at the second junction, the more it had been stretched, resulting in fewer blood cells being sorted into the new aliquot. Results using sorted dye aliquots seemed promising (see Figure 4.2C), but the small size of the side channels needed resulted in clogging and potential cell loss. Figure 4.2 shows the results of the flow stretcher stretching tests, both a straight channel flow stretcher and a flow stretcher where herringbone features were

used to spread the aliquot laterally across the channel. While the flow stretcher was not used in the final system, the herringbone features employed are used in the final iteration.

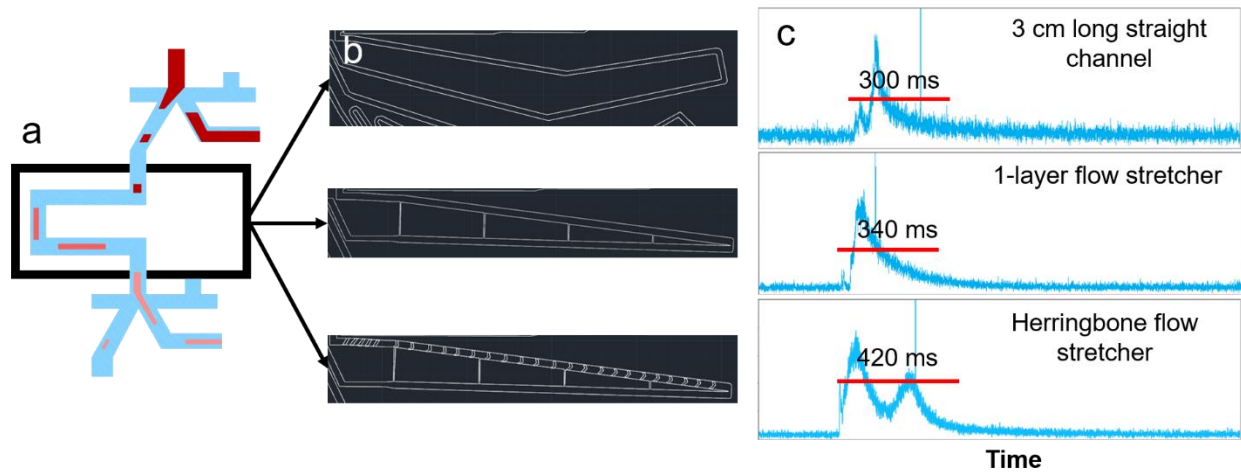


**Figure 4.2** Different designs tested to stretch the aliquot. **a** In all chips, the design was the same except for the channel separating the two junctions, shown in the rectangle. **b** AutoCAD images of four of the designs tested. **c** Data traces from the second sorting junction of aliquots containing PE dye and a fluorescent bead, which was used to trigger the sort in the first junction. The length of the dye aliquot in this junction can be used as an estimate of the stretching done by that design.

The second strategy involved weirs, sections where the channel was briefly reduced in height to 5-30  $\mu\text{m}$  tall, placed along the channel separating the junctions. It was hypothesized that the CTCs, being larger and less deformable, would be substantially slowed down at the weirs, and the other blood cells would continue. However, initial tests showed cells clogging at the weirs and this idea was put aside due to fear of cells loss. Another weir-like structure was tested, where a weir filter was employed laterally across the channel, with slits of 30-35  $\mu\text{m}$ . This design also had cell clogging, as seen in Figure 4.3. This clogging seemed to be caused by clusters of cells. CTC clusters have recently been studied as a potentially source of metastasis<sup>75</sup>,

therefore due to these cell clogging issues in both the flow stretcher and the weir designs, our focus moved to features that did not include any constrictions.

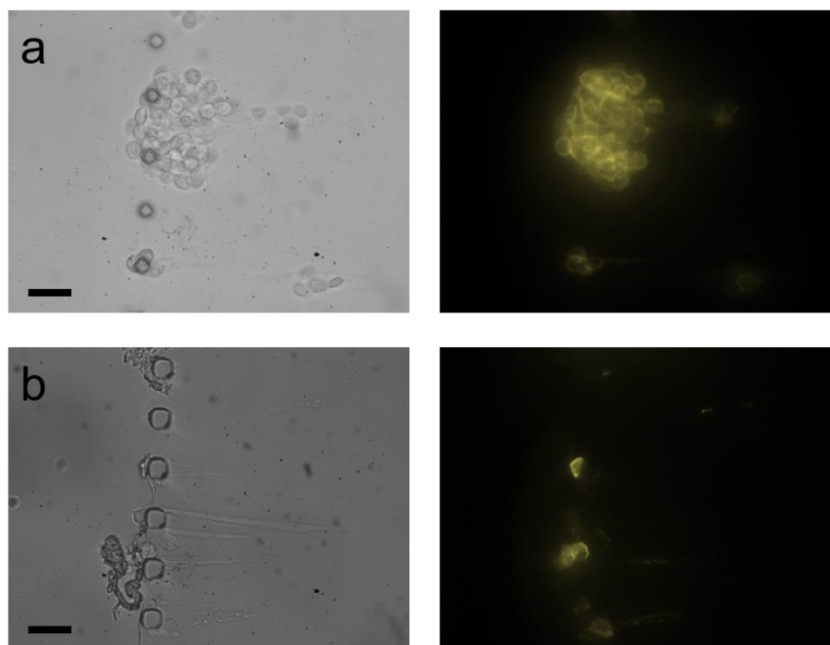


**Figure 4.3** Images of weir filter tests. Scale bars are 35  $\mu\text{m}$ . PE-anti-EpCAM labeled MCF7 cells were flowed through the channel at a flow rate of 180  $\mu\text{l}/\text{min}$ . **a** Left image is a brightfield picture of a section the channel. The slits span the length of the channel, and are 35  $\mu\text{m}$  wide. The right image is a fluorescent image of the PE labeled cells stuck in the features. **b** Left image is a brightfield picture of a section of the channel, in this case with 30  $\mu\text{m}$  wide slits. The right image is a fluorescent image of the PE labeled cells stuck in the features.

Finally, we employed a chaotic mixing design using herringbone features at the beginning of the separation channel, to spread the aliquot out laterally before it traveled down the rest of the channel. This design was implemented first in the flow stretcher to improve performance, but after results indicated channel clogging could cause cell loss, it was added to the 5.5 cm and 8.8 cm channel designs, with herringbones used along the first 0.7 cm of the channel. Herringbones were first presented by Whitesides and coworkers in 2002<sup>74</sup> and are attractive as a mixing strategy for several reasons. First, they are simple to fabricate, requiring

only one additional layer of SU-8 microfabrication and not requiring any valves or complicated features. Second, they have been demonstrated to tunable to a wide variety of applications<sup>76</sup>.

Finally, they do not add constrictions where cells could be trapped.

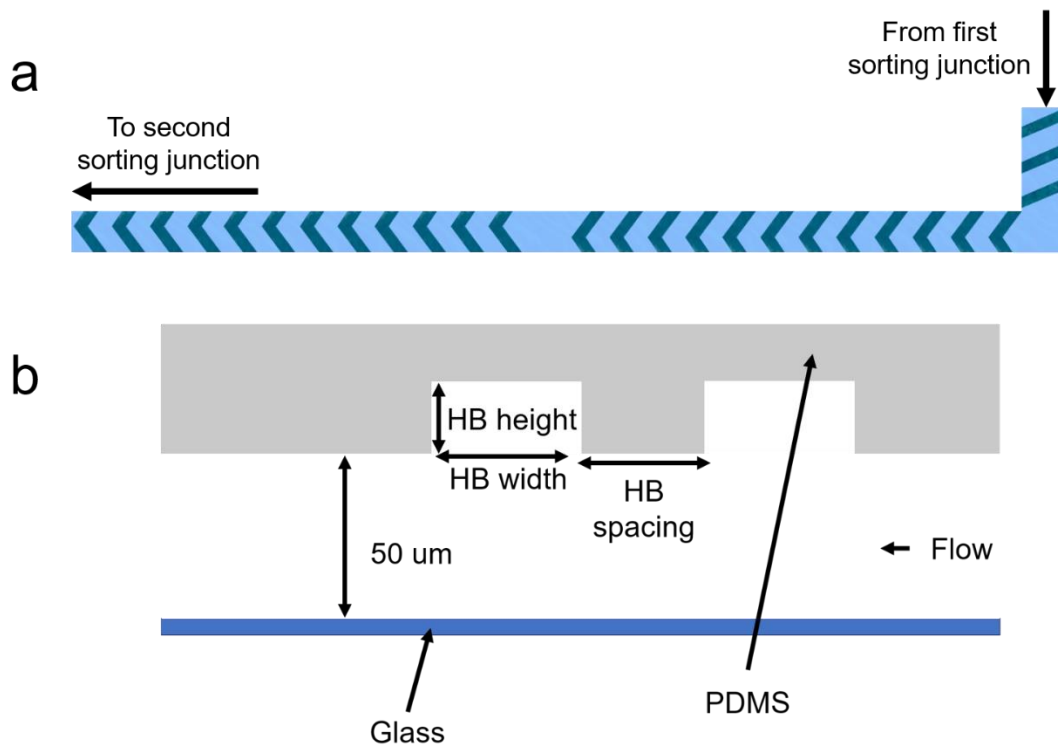


**Figure 4.4** **a** Scheme of the herringbone structure employed in the sequential sorting chip. There are three sections of herringbones: three at the beginning, 12 more angled slightly in and 12 more angled slightly out. **b** Cross section of the herringbone channel, showing the important dimensions. For the herringbone chip used, the herringbone height was  $30\ \mu\text{m}$ . The first section of straight herringbones were  $80\ \mu\text{m}$  wide and spaced  $95\ \mu\text{m}$  apart. The second and third sections of herringbones were  $70\ \mu\text{m}$  wide and spaced  $180\ \mu\text{m}$  apart.

We employed a herringbone design consisting of three sections of herringbones (see figure 4.4A): three initial herringbones angled from the inner wall to the outer wall, since we have observed the aliquot traveling primarily down the inner wall; a section of 12 herringbones staggered with the center more towards the outer wall; and then 12 herringbones staggered the opposite direction. The herringbone height was 30  $\mu\text{m}$ . The first section of straight herringbones were 80  $\mu\text{m}$  wide and spaced 95  $\mu\text{m}$  apart. The second section of herringbones were 70  $\mu\text{m}$  wide and spaced 180  $\mu\text{m}$  apart. The mixing section was 0.7 cm long, with a 4.8 cm or 8.1 cm straight channel immediately after. This design allows sufficient mixing, so that the cells, rather than traveling in a plug long the outer wall, are separated laterally across the channel. The long section of straight channel would then allow the cells to further separate longitudinally, as the cells near the center of the channel would travel faster than the cells on the outer edges. The 5.5 cm herringbone (HB) chip yielded 30% purity when tested as previously described, similar to the 8.8 cm none HB chip. The 8.8 cm HB chip yielded 70% purity. This means that for each sorted CTC in the first junction, there is on average <1 white blood cells when is sorted again in the second junction. Without the second sort, there are approximately 100 white blood cells sorted with each CTC. With an average of 100 MCF7 cells sorted, there were about 43 white blood cells collected after the second sort. Since the total sorted volume is about 1 ml, this corresponds to a white blood cell depletion rate of  $1.2 \times 10^5$  or 5.1 log ( $5 \times 10^6$  white blood cells/ml in whole blood versus 43 white blood cells/ml in the sorted volume). It is possible that more herringbones with an even longer channel could potentially improve this further. The purity results obtained by the designs tested are summarized in Table 4.1.

Design	Purity (CTCs/total nucleated cells)
1-stage eDAR	1%
3 cm Channel	17%
5.5 cm Channel	21%
8.8 cm Channel	32%
5.5 cm Channel + HB	30%
8.8 cm Channel + HB	70%

**Table 4.1** Purity results for three sequential eDAR designs compared to 1-stage eDAR.

#### 4.4.4 *Cells can be collected and enumerated in a 96-well plate.*

For this method to be clinically useful, cells needed to be collected in a way they could be easily enumerated, and spike-in recoveries, the traditional method of validating CTC isolation techniques, needed to be performed. The eDAR platform has previously been validated with recoveries from different cells lines as well as clinical samples. This method introduces two new elements where cell loss could occur: the second sorting junction and the 96-well plate collection. Thus, recoveries were performed to verify that these elements do not generate cell loss.

Recoveries were conducted with pre-labeled MCF7 cells for simplicity. Previous tests of our in-blood cell labeling steps have been conducted<sup>7</sup>, so for this report we decided to isolate only the features that are new to the system. The first of these is the new fluidic scheme: including two sorting junctions on a chip. Flow was balanced in a similar manner to previous chips, now with sheath flow pressures adjusted for three positions: (1) solenoid one and two off

with flow down the first waste channel (the first frame in both Figure 4.5a and b), (2) solenoid one open and solenoid two closed with flow down the first collection channel (shown in Figure 4.5a), and (3) solenoid one closed and solenoid two open to collect cells down the second collection (Figure 4.5b). Sorting on the sequential chip was more stable due to the absence of the on-chip filter introducing potential clogs.

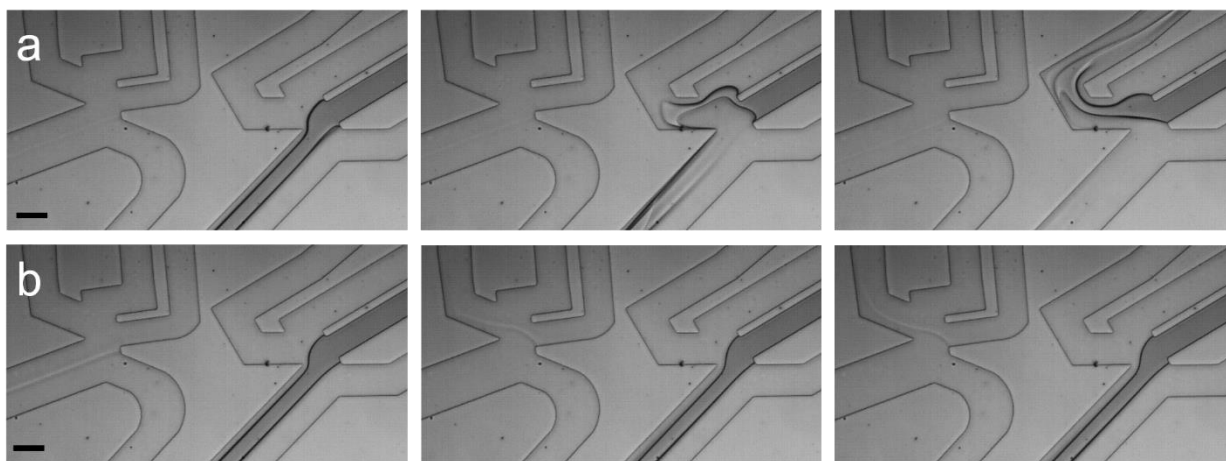


**Figure 4.5** Images of the sequential sorting fluidics scheme. Scale bars are 200  $\mu\text{m}$ . Sorted solution is 30% glycerol solution (25% w/w glycerol in Isoton) and 70% green food dye **a** Three frames showing sorting in the first junction, from left to right: no solenoid open, solenoid opens and flows starts to move to the left, flow is fully down the collection channel. **b** Three frames showing sorting the second junction, from left to right: no solenoid open, solenoid opens and flows starts to move to the left, flow is fully down the collection channel

To collect the PE-anti-EpCAM labeled MCF7 cells after they are sorted at the second junction, pre-treated tubing was inserted into the collection outlet after sorting was established and the outlet of the tubing was mounted above a pre-treated 96 well plate. Tubing and the 96-well plate for collection were pre-treated with a solution of 1% BSA + 0.05% Tween20 in Isoton to prevent cell sticking. The output volume was collected in a well until it reached  $\sim 250 \mu\text{l}$ , then

the tubing was manually moved to the next well. The total output for the sorting of 0.5 ml of blood was ~4 wells or ~1ml. To enumerate the cells in the wells, the plate was spun down on a plate centrifuge at 450 rcf for 10 min to isolate all the cells to the bottom of the well. Cells could then be counted on a fluorescent microscope with a 20X, 0.75 NA objective. Figure 4.6 shows MCF7 cells labeled with PE-anti-EpCAM imaged after sorting. Two cell clusters are shown to illustrate that the sequential eDAR system is capable of isolating clusters, which could be an important tool for studying metastasis<sup>77</sup>. At this stage, if further labeling was required, the supernatant could be removed to a desired labeling volume and antibodies or fixing/permeabilization solutions added. To verify that this step would not introduce cell loss, we spun the cells an additional time, removed the supernatant, added 200  $\mu$ l isoton buffer + 0.1% BSA, spun the plate again and recounted the well. No cell loss was observed. Recoveries for all three designs (3 cm channel, 5.5 cm channel and 5.5 cm channel with herringbones) averaged 91%, indicating that minimal cell loss is introduced with the new design.

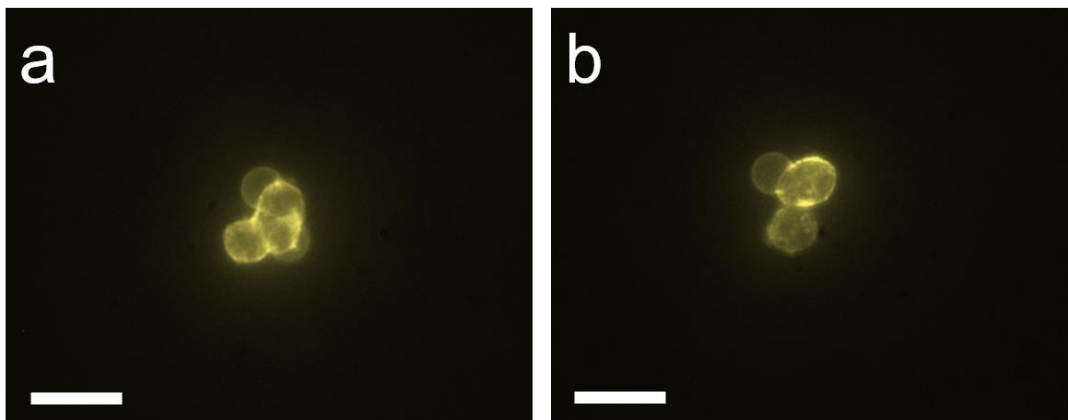


**Figure 4.6** Images of MCF7 cells, labeled with PE-anti-EpCAM and sorted on sequential eDAR into a 96-well plate. Images are taken with a 20X, 0.75 NA objective in yellow fluorescence. Scale represent 40  $\mu$ m. **a** Cluster of four cells. **b** Cluster of three cells

## 4.5 CONCLUSION

We have presented a sequential sorting based CTC isolation platform. This is a modification of our previously published platform, eDAR, and thus makes use of the advantages of our previous work. These includes high recoveries with spiked-in cells lines and well as clinical validation, including improved performance over the FDA approved CellSearch™. eDAR has also been calibrated and shown to be highly sensitive to cells which have undergone the epithelial-to-mesenchymal transition and express low levels of traditional CTC markers. These cells are thought the be more metastatic and are an important area for future research.

It is also a significant improvement over our previous work for two reasons. One, we have improved the purity of our system, from 1% from our previous design, to up to 70%. This was achieved by adding a second sorting junction on the same chip, and then adding passive mixing designs between the two junctions to stretch and dilute the sorted aliquot. Second, we have moved collection off-chip while still maintaining high recoveries. Cells are now collected and enumerated in a 96-well plate, making eDAR more amenable to downstream analyses such as PCR or DNA sequencing. Previously eDAR was capable of multiple labeling steps by implementing a consecutive bleaching and re-labeling scheme. However, only so much information can be obtained from antibody labeling, and opening our platform to further downstream analysis is an important step forward. While this method does not produce one-cell-per-well at the time of this report, it is amenable to coupling with an automated dispensing system. This would allow an all-in-one platform for CTC detection, enumeration and analysis that could access the most dangerous, metastatic cells missed by many methods.

## BIBLIOGRAPHY

1. Cohen, S. J. *et al.* Relationship of circulating tumor cells to tumor response, progression-free survival, and overall survival in patients with metastatic colorectal cancer. *J. Clin. Oncol.* **26**, 3213–21 (2008).
2. Paterlini-Brechot, P. & Benali, N. L. Circulating tumor cells (CTC) detection: clinical impact and future directions. *Cancer Lett.* **253**, 180–204 (2007).
3. Powell, A. A. *et al.* Single cell profiling of circulating tumor cells: transcriptional heterogeneity and diversity from breast cancer cell lines. *PLoS One* **7**, e33788 (2012).
4. Kalluri, R. & Weinberg, R. A. Review series The basics of epithelial-mesenchymal transition. *J. Clin. Invest.* **119**, 1420–1428 (2009).
5. Bonnomet, A. *et al.* Epithelial-to-mesenchymal transitions and circulating tumor cells. *J. Mammary Gland Biol. Neoplasia* **15**, 261–73 (2010).
6. Driemel, C. *et al.* Context-dependent adaption of EpCAM expression in early systemic esophageal cancer. *Oncogene* **33**, 4904–15 (2014).
7. Zhao, M. *et al.* New Generation of Ensemble-Decision Aliquot Ranking Based on Simplified Microfluidic Components for Large-Capacity Trapping of Circulating Tumor Cells. *Anal. Chem.* **85**, 9671–9677 (2013).
8. Mitri, Z., Constantine, T. & O'Regan, R. The HER2 Receptor in Breast Cancer: Pathophysiology, Clinical Use, and New Advances in Therapy. *Chemother. Res. Pract.* **2012**, 1–7 (2012).
9. Nicholson, R. ., Gee, J. M. . & Harper, M. . EGFR and cancer prognosis. *Eur. J. Cancer* **37**, 9–15 (2001).
10. Dharmasiri, U., Witek, M. A., Adams, A. A. & Soper, S. A. Microsystems for the capture of low-abundance cells. *Annu. Rev. Anal. Chem.* **3**, 409–31 (2010).
11. Alunni-Fabbroni, M. & Sandri, M. T. Circulating tumour cells in clinical practice: Methods of detection and possible characterization. *Methods* **50**, 289–97 (2010).
12. Gross, H. J., Verwer, B., Houck, D., Hoffman, R. A. & Recktenwald, D. Model study detecting breast cancer cells in peripheral blood mononuclear cells at frequencies as low as 10<sup>(-7)</sup>. *Proc. Natl. Acad. Sci. U. S. A.* **92**, 537–541 (1995).
13. Hsieh, H. Ben *et al.* High speed detection of circulating tumor cells. *Biosens. Bioelectron.* **21**, 1893–9 (2006).

14. Krivacic, R. T. *et al.* A rare-cell detector for cancer. *Proc. Natl. Acad. Sci. U. S. A.* **101**, 10501–10504 (2004).
15. Allard, W. J. *et al.* Tumor cells circulate in the peripheral blood of all major carcinomas but not in healthy subjects or patients with nonmalignant diseases. *Clin. Cancer Res.* **10**, 6897–6904 (2004).
16. Riethdorf, S. *et al.* Detection and HER2 expression of circulating tumor cells: prospective monitoring in breast cancer patients treated in the neoadjuvant GeparQuattro trial. *Clin. Cancer Res.* **16**, 2634–45 (2010).
17. Balasubramanian, P. *et al.* Confocal images of circulating tumor cells obtained using a methodology and technology that removes normal cells. *Mol. Pharm.* (2009). doi:10.1021/mp9000519
18. Nagrath, S. *et al.* Isolation of rare circulating tumour cells in cancer patients by microchip technology. *Nature* **450**, 1235–1239 (2007).
19. Dharmasiri, U. *et al.* High-Throughput Selection , Enumeration , Electrokinetic Manipulation , and Molecular Profiling of Low-Abundance Circulating Tumor Cells Using a Microfluidic System ( 1 ) Center for Bio-Modular Multi-Scale Systems , Louisiana State University , 8000 G . S. *Anal. Chem.* **83**, 2301–2309 (2011).
20. Wang, S. *et al.* Highly efficient capture of circulating tumor cells by using nanostructured silicon substrates with integrated chaotic micromixers. *Angew. Chemie - Int. Ed.* **50**, 3084–3088 (2011).
21. Yu, L. *et al.* Advances of lab-on-a-chip in isolation, detection and post-processing of circulating tumour cells. *Lab Chip* **13**, 3163–82 (2013).
22. Zheng, S. *et al.* Membrane microfilter device for selective capture, electrolysis and genomic analysis of human circulating tumor cells. *J. Chromatogr. A* **1162**, 154–61 (2007).
23. Kahn, H. J. *et al.* Enumeration of circulating tumor cells in the blood of breast cancer patients after filtration enrichment: correlation with disease stage. *Breast Cancer Res. Treat.* **86**, 237–247 (2004).
24. Kuo, J. S. *et al.* Deformability considerations in filtration of biological cells. *Lab Chip* **10**, 837–42 (2010).
25. Pinzani, P. *et al.* Isolation by size of epithelial tumor cells in peripheral blood of patients

- with breast cancer: correlation with real-time reverse transcriptase-polymerase chain reaction results and feasibility of molecular analysis by laser microdissection. *Hum. Pathol.* **37**, 711–8 (2006).
26. Lin, H. K. *et al.* Portable filter-based microdevice for detection and characterization of circulating tumor cells. *Clin. Cancer Res.* **16**, 5011–8 (2010).
  27. Coumans, F. A. W., van Dalum, G., Beck, M. & Terstappen, L. W. M. M. Filter Characteristics Influencing Circulating Tumor Cell Enrichment from Whole Blood. *PLoS One* **8**, (2013).
  28. Schiro, P. G. *et al.* Sensitive and high-throughput isolation of rare cells from peripheral blood with ensemble-decision aliquot ranking. *Angew. Chem. Int. Ed. Engl.* **51**, 4618–22 (2012).
  29. Zhao, M. *et al.* An automated high-throughput counting method for screening circulating tumor cells in peripheral blood. *Anal. Chem.* **85**, 2465–71 (2013).
  30. Georgoulas, V. *et al.* Trastuzumab decreases the incidence of clinical relapses in patients with early breast cancer presenting chemotherapy-resistant CK-19mRNA-positive circulating tumor cells: results of a randomized phase II study. *Ann. Oncol.* **23**, 1744–50 (2012).
  31. Adams, A. A. *et al.* Highly efficient circulating tumor cell isolation from whole blood and label-free enumeration using polymer-based microfluidics with an integrated conductivity sensor. *J. Am. Chem. Soc.* **130**, 8633–8641 (2008).
  32. Zhao, M., Wei, B., Nelson, W. C., Schiro, P. G. & Chiu, D. T. Simultaneous and selective isolation of multiple subpopulations of rare cells from peripheral blood using ensemble-decision aliquot ranking (eDAR). *Lab Chip* **15**, 3391–3396 (2015).
  33. Buganim, Y., Faddah, D. A. & Jaenisch, R. Mechanisms and models of somatic cell reprogramming. *Nat. Rev. Genet.* **14**, 427–439 (2013).
  34. Rubakhin, S. S., Lanni, E. J. & Sweedler, J. V. Progress toward single cell metabolomics. *Curr. Opin. Biotechnol.* **24**, 95–104 (2013).
  35. Kovarik, M. L., Shah, P. K., Armistead, P. M. & Allbritton, N. L. Microfluidic chemical cytometry of peptide degradation in single drug-treated acute myeloid leukemia cells. *Anal. Chem.* **85**, 4991–4997 (2013).
  36. Marjanovic, N. D., Weinberg, R. A. & Chaffer, C. L. Cell plasticity and heterogeneity in

- cancer. *Clin. Chem.* **59**, 168–179 (2013).
37. Swanton, C. Intratumor heterogeneity: Evolution through space and time. *Cancer Res.* **72**, 4875–4882 (2012).
  38. Walling, M. A. & Shepard, J. R. E. Cellular heterogeneity and live cell arrays. *Chem. Soc. Rev.* **40**, 4049–4076 (2011).
  39. Lecault, V., White, A. K., Singhal, A. & Hansen, C. L. Microfluidic single cell analysis: From promise to practice. *Curr. Opin. Chem. Biol.* **16**, 381–390 (2012).
  40. Cetin, B. & Li, D. Dielectrophoresis in microfluidics technology. *Electrophoresis* **32**, 2410–2427 (2011).
  41. Gagnon, Z. R. Cellular dielectrophoresis: Applications to the characterization, manipulation, separation and patterning of cells. *Electrophoresis* **32**, 2466–2487 (2011).
  42. Martinez-Duarte, R. Microfabrication technologies in dielectrophoresis applications-A review. *Electrophoresis* **33**, 3110–3132 (2012).
  43. Shafiee, H., Sano, M. B., Henslee, E. A., Caldwell, J. L. & Davalos, R. V. Selective isolation of live/dead cells using contactless dielectrophoresis (cDEP). *Lab Chip* **10**, 438 (2010).
  44. Sankaran, B. *et al.* Dielectrophoretic capture of mammalian cells using transparent indium tin oxide electrodes in microfluidic systems. *Electrophoresis* **29**, 5047–5054 (2008).
  45. and, B. M. T. & Voldman\*, J. A Scalable Addressable Positive-Dielectrophoretic Cell-Sorting Array. **77**, 7976–7983 (2005).
  46. Faenza, A. *et al.* High Yield Patterning of Single Cells from Extremely Small Populations. *Anal. Chem.* **85**, 3446–3453 (2013).
  47. Kalisky, T., Blainey, P. & Quake, S. R. Genomic Analysis at the Single-Cell Level. *Annu. Rev. Genet.* **45**, 431–445 (2011).
  48. Martinez-Duarte, R., Renaud, P. & Madou, M. J. A novel approach to dielectrophoresis using carbon electrodes. *Electrophoresis* **32**, 2385–2392 (2011).
  49. Huang, K.-W., Wu, Y.-C., Lee, J.-A. & Chiou, P.-Y. Microfluidic integrated optoelectronic tweezers for single-cell preparation and analysis. *Lab Chip* **13**, 3721–3727 (2013).
  50. Valley, J. K. *et al.* Parallel single-cell light-induced electroporation and dielectrophoretic manipulation. *Lab Chip* **9**, 1714–1720 (2009).

51. Hlushkou, D., Perdue, R. K., Dhopeswarkar, R., Crooks, R. M. & Tallarek, U. Electric field gradient focusing in microchannels with embedded bipolar electrode. *Lab Chip* **9**, 1903–1913 (2009).
52. Laws, D. R., Hlushkou, D., Perdue, R. K., Tallarek, U. & Crooks, R. M. Bipolar electrode focusing: Simultaneous concentration enrichment and separation in a microfluidic channel containing a bipolar electrode. *Anal. Chem.* **81**, 8923–8929 (2009).
53. Anand, R. K., Sheridan, E., Hlushkou, D., Tallarek, U. & Crooks, R. M. Bipolar electrode focusing: tuning the electric field gradient. *Lab Chip* **11**, 518–527 (2011).
54. Anand, R. K., Sheridan, E., Knust, K. N. & Crooks, R. M. Bipolar electrode focusing: Faradaic ion concentration polarization. *Anal. Chem.* **83**, 2351–2358 (2011).
55. Perdue, R. K., Laws, D. R., Hlushkou, D., Tallarek, U. & Crooks, R. M. Bipolar electrode focusing: The effect of current and electric field on concentration enrichment. *Anal. Chem.* **81**, 10149–10155 (2009).
56. Khoshmanesh, K., Nahavandi, S., Baratchi, S., Mitchell, A. & Kalantar-zadeh, K. Dielectrophoretic platforms for bio-microfluidic systems. *Biosens. Bioelectron.* **26**, 1800–1814 (2011).
57. Chow, K. F., Mavr e, F., Crooks, J. A., Chang, B. Y. & Crooks, R. M. A large-scale, wireless electrochemical bipolar electrode microarray. *J. Am. Chem. Soc.* **131**, 8364–8365 (2009).
58. Mavr e, F. *et al.* Bipolar electrodes: A useful tool for concentration, separation, and detection of analytes in microelectrochemical systems. *Anal. Chem.* **82**, 8766–8774 (2010).
59. Mavre, F. *et al.* A Theoretical and Experimental Framework for Understanding Electrogenenerated Chemiluminescence (ECL) Emission at Bipolar Electrodes. *Anal. Chem.* **81**, 6218–6225 (2009).
60. Knust, K. N., Hlushkou, D., Anand, R. K., Tallarek, U. & Crooks, R. M. Electrochemically mediated seawater desalination. *Angew. Chemie - Int. Ed.* **52**, 8107–8110 (2013).
61. Somiari, S. *et al.* Theory and in Vivo Application of Electroporative Gene Delivery. *Mol. Ther.* **2**, 178–187 (2000).
62. McDonald, J. C. *et al.* Fabrication of microfluidic systems in poly(dimethylsiloxane).

- Electrophoresis* **21**, 27–40 (2000).
63. Hellmich, W. *et al.* Poly ( oxyethylene ) Based Surface Coatings for Poly ( dimethylsiloxane ) Microchannels. *Langmuir* **21**, 7551–7557 (2005).
  64. Wiklund, M. *et al.* Ultrasonic standing wave manipulation technology integrated into a dielectrophoretic chip. *Lab Chip* **6**, 1537–1544 (2006).
  65. Lvovich, V. F. *Impedance Spectroscopy Applications to Electrochemical and Dielectric Phenomena*. (John Wiley and Sons, 2012).
  66. Zhao, M., Wei, B. & Chiu, D. T. Imaging multiple biomarkers in captured rare cells by sequential immunostaining and photobleaching. *Methods* **64**, 108–113 (2013).
  67. Johnson, E. S., Anand, R. K. & Chiu, D. T. Improved detection by ensemble decision aliquot ranking (eDAR) of circulating tumor cells with low numbers of a targeted surface antigen. *Anal. Chem.* **87**, 9389–9395 (2015).
  68. Welsh, J. The use of FACS for the selection of cell lines with superior productivity characteristics. *Powerpoint* 1–30 (2007).
  69. Hou, H. W. *et al.* Isolation and retrieval of circulating tumor cells using centrifugal forces. *Sci. Rep.* **3**, 1–8 (2013).
  70. Warkiani, M. E. *et al.* Ultra-fast, label-free isolation of circulating tumor cells from blood using spiral microfluidics. *Nat. Protoc.* **11**, 134–148 (2015).
  71. Li, M. & Anand, R. K. High-Throughput Selective Capture of Single Circulating Tumor Cells by Dielectrophoresis at a Wireless Electrode Array. *J. Am. Chem. Soc.* (2017). doi:10.1021/jacs.7b03288
  72. Balic, M. *et al.* Comparison of two methods for enumerating circulating tumor cells in carcinoma patients. *Cytom. Part B - Clin. Cytom.* **68**, 25–30 (2005).
  73. Park, M. H. *et al.* Enhanced Isolation and Release of Circulating Tumor Cells Using Nanoparticle Binding and Ligand Exchange in a Microfluidic Chip. *J. Am. Chem. Soc.* **139**, 2741–2749 (2017).
  74. Stroock, A. D. *et al.* Chaotic Mixer for Microchannels. *Science (80-. )*. **295**, 647–651 (2002).
  75. Pantel, K. & Speicher, M. R. The biology of circulating tumor cells. *Oncogene* **35**, 1216–1224 (2016).
  76. Manda S. Williams, Kenneth J. Longmuir, and P. Y. A practical guide to the staggered

herringbone mixer. *Lab Chip* **8**, 1121–1129 (2008).

77. Au, S. H. *et al.* Microfluidic Isolation of Circulating Tumor Cell Clusters by Size and Asymmetry. *Sci. Rep.* **7**, 2433 (2017).

# CURRICULUM VITAE

## Education

<b>PhD</b>	University of Washington, Seattle, WA Analytical Chemistry, Advisor Daniel T. Chiu Thesis Title: "Microfluidic Tools for Detecting and Isolating Cancer Cells"	Expected Summer 2017
<b>MS</b>	University of Washington, Seattle, WA Analytical Chemistry, Advisor Daniel T. Chiu	2012
<b>BA</b>	University of Colorado, Boulder, CO Biochemistry	2010

## Professional Experience

<b>Lecturer</b> , Department of Chemistry Seattle University	Winter 2017
<b>Graduate Teaching Assistant</b> , Department of Chemistry University of Washington	2010-2016
<b>Graduate Research Assistant</b> , Department of Chemistry University of Washington	2010-2017
<b>Undergraduate Student Researcher</b> , Department of Chemistry University of Colorado	2009-2010
<b>Learning Assistant</b> , STEM Colorado University of Colorado	2009-2010
<b>Tutor</b> , Housing and Dining Services University of Colorado	2009-2010

## Research Skills

### Graduate Research

**Dr. Daniel T. Chiu, University of Washington**

Developing devices for the detection and isolating circulating tumor cells from blood

Related Skills:

- Fluorescence microscopy
- Soft lithography
- Cell culture
- Flow Cytometry

**Undergraduate Research**  
**Dr. Josef Michl, University of Colorado**

Studied triplet spectra and fluorescence anisotropy of small organic fluorophores

Related Skills:

- Fluorescence spectroscopy
- Freeze-pump-thaw cycling

**Publications**

1. Kuo, C.T.; Thompson, A. M.; Gallina, M. E.; Ye, F.; *Johnson, E. S.*; Sun, W.; Zhao, M.; Yu, J.; Wu, I.; Fujimoto, B.; DuFort, C. C.; Carlson, M. A.; Hingorani, S. R.; Paguirigan, A. L.; Radish, J. P.; and Chiu, D. T. Optical painting and fluorescence activated sorting of single adherent cells labelled with photoswitchable Pdots. *Nature Communications*, 2016, 7, 11468.
2. *Johnson, E. S.*; Anand, R. K.; and Chiu, D. T. Improved detection by ensemble decision aliquot ranking (eDAR) of circulating tumor cells with low numbers of a targeted surface antigen. *Anal. Chem.* 2015, 87, 9389-9395.
3. Anand, R. K.; *Johnson, E. S.*; Chiu, D. T. Negative Dielectrophoretic Capture and Repulsion of Single Cells at a Bipolar Electrode: The Impact of Faradaic Ion Enrichment and Depletion. *JACS*, 2015, 137, 776-783.
4. Zhao, M.; Nelson, W. C.; Wei, B.; Schiro, P. G.; Hakimi, B. M.; *Johnson, E. S.*; Anand, R. K.; Gyurkey, G. S.; White, L. M.; Whiting, S. H. Coveler, A. L.; Chiu, D. T. New generation of ensemble-decision aliquot ranking based on simplified microfluidic components for large-capacity trapping of circulating tumor cells. *Anal Chem.* 2013, 85, 9671-9677